Linear Time-Periodic Modeling, Examination, and Performance Enhancement of Grid Synchronization Systems with DC Component Rejection/Estimation Capability

Golestan, Saeed; Guerrero, Josep M.; Vasquez, Juan C.; Abusorrah, Abdullah M.; Al-Turki, Yusuf

Published in:
IEEE Transactions on Power Electronics

DOI (link to publication from Publisher):
10.1109/TPEL.2020.3018584

Publication date:
2021

Document Version
Accepted author manuscript, peer reviewed version

Linear Time-Periodic Modeling, Examination, and Performance Enhancement of Grid Synchronization Systems With DC Component Rejection/Estimation Capability

Saeed Golestan, *Senior Member, IEEE*, Josep M. Guerrero, *Fellow, IEEE*, Juan C. Vasquez, *Senior Member, IEEE*, Abdullah M. Abusorrah, *Senior Member, IEEE*, and Yusuf Al-Turki, *Senior Member, IEEE*

***Abstract*—The dc component, which may be caused by different factors in the grid voltage, is one of the disturbances that may severely affect the performance of grid synchronization systems and, therefore, grid-tied power converters. In the phase-locked loop (PLL) and frequency-locked loop (FLL) based grid synchronization systems, which this paper focuses on, some solutions to deal with this challenge have been proposed in the literature. One of the best available solutions is adding dc rejection/estimation loop(s) to a standard PLL and FLL structure. This approach provides an estimation of the dc component and at the same time makes the PLL and FLL immune to disturbance effects of the dc component. Despite their implementation simplicity, no linear model for the grid synchronization systems with the dc rejection/estimation capability has yet been presented. The main aim of this paper is to fill this research gap. It will be shown that developing such models facilitates the examination and even the performance enhancement of the grid synchronization systems under study.**

***Index Terms*—DC component, frequency-locked loop (FLL), linear time-invariant (LTI), linear time-periodic (LTP), phase-locked loop (PLL), reduced-order generalized integrator (ROGI), second-order generalized integrator (SOGI), single-phase systems, synchronization, three-phase systems.**

I. Introduction

FREQUENCY-LOCKED loops (FLLs) [1], [2] and phase-locked loops (PLLs) [3], [4] are two popular options for the grid synchronization of power converters. From the control point of view, they are both nonlinear feedback control systems. However, they are implemented in different ways.

Generally speaking, designing PLLs is based on transferring the grid voltage signal(s) into a synchronous reference frame (SRF) and, therefore, it involves computing sine and cosine functions. Fig. 1(a) illustrates the block diagram of a standard three-phase PLL, which is known as the conventional SRF-PLL [5], [6]. In the conventional SRF-PLL, the three-phase grid voltage signals are transferred into an SRF with the rotating angle $\hat{\theta}_1$, where $\hat{\theta}_1$ is an estimation of the phase angle of the fundamental-frequency positive-sequence (FFPS) component of the grid voltage. Therefore, the signal v_d in the SRF-PLL provides an estimation of the amplitude of the FFPS component, and the signal v_q provides the error between the actual and estimated phase angles. This error is regulated to zero using a loop controller, which is a proportional-integral (PI) regulator.

Because of the lack of multiple input signals, designing single-phase PLLs is often more complicated than the three-phase ones [7]. To deal with this difficulty, often a fictitious signal with the same amplitude and 90° difference compared to the fundamental component of the single-phase input signal is created [4], [8], [9]. In the simplest possible case, this fictitious signal is directly generated using the estimated amplitude and phase angle by the single-phase PLL. The resulting PLL is known as the synthesis circuit PLL [10], which is mathematically equivalent to the enhanced PLL (EPLL) structure in Fig. 2(a) [11]. Notice that the governing differential equations of the EPLL may also be directly obtained using the gradient descent method.

Designing FLLs is quite different from PLLs. The basic idea in designing FLLs is using a band-pass filter (BPF) to extract the grid voltage fundamental component and a frequency detector to make this BPF frequency-adaptive. In three-phase applications, the reduced-order generalized integrator-based FLL (ROGI-FLL) [see Fig. 3(a)] is a standard structure [2], [12]–[15]. The ROGI-FLL includes a complex-coefficient BPF,[1] which is realized by using a ROGI centered at the fundamental frequency in a unity feedback loop, and a frequency detector to adapt the center of the ROGI to frequency changes. In single-phase applications, the second-order generalized integrator-based FLL (SOGI-FLL) [see Fig. 4(a)] is a standard structure [1], [17]. The SOGI-FLL provides an estimation of the grid voltage fundamental component and its 90° phase-shifted version by including a SOGI in a unity feedback loop. A

Manuscript received March 18, 2020; revised June 26, 2020; accepted August 15, 2020. This work was supported in part by the Deanship of Scientific Research (DSR), King Abdulaziz University, Jeddah and in part by VILLUM FONDEN under the VILLUM Investigator Grant (no. 25920): Center for Research on Microgrids (CROM); www.crom.et.aau.dk.

S. Golestan, J. M. Guerrero, and J. C. Vasquez are with the Department of Energy Technology, Aalborg University, Aalborg DK-9220, Denmark (e-mail: sgd@et.aau.dk; joz@et.aau.dk; juq@et.aau.dk).

A. M. Abusorrah and Y. Al-Turki are with the Department of Electrical and Computer Engineering, Faculty of Engineering, and Center of Research Excellence in Renewable Energy and Power Systems, King Abdulaziz University, Jeddah, Saudi Arabia (e-mail: aabusorrah@kau.edu.sa; yaturki@yahoo.com).

Color versions of one or more of the figures in this paper are available online at http://ieeexplore.ieee.org.

[1] A complex-coefficient filter, contrary to the real-coefficient one, has an asymmetrical frequency-response around zero Hz [16].

This article has been accepted for publication in a future issue of this journal, but has not been fully edited. Content may change prior to final publication. Citation information: DOI 10.1109/TPEL.2020.3018584, IEEE Transactions on Power Electronics

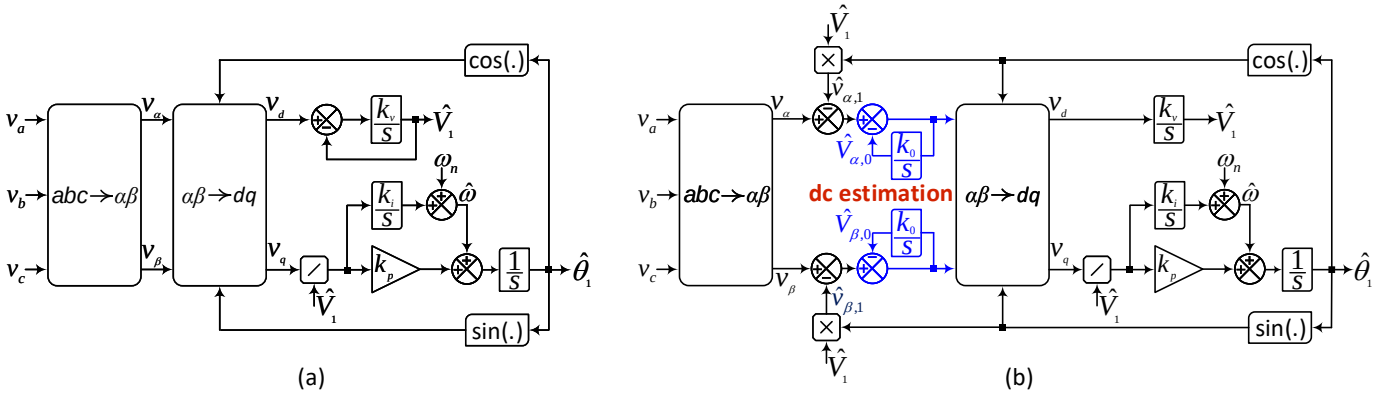

Fig. 1. (a) Conventional SRF-PLL. (b) Modified SRF-PLL (mSRF-PLL). k_p, k_i, k_v, and k_0 are the control parameters. v_a, v_b, and v_c denote the three-phase grid voltage signals, and v_α and v_β are the grid voltage signals in the $\alpha\beta$ frame. $\hat{v}_{\alpha,1}$ and $\hat{v}_{\beta,1}$ are estimations of the fundamental component of v_α and v_β, respectively. $\hat{V}_{\alpha,0}$ and $\hat{V}_{\beta,0}$ are estimations of the dc component of the signals v_α and v_β, respectively. $\hat{V}_1$, $\hat{\theta}_1$, and $\hat{\omega}$ are estimations of the amplitude, phase angle, and angular frequency of the grid voltage fundamental component, respectively. ω_n is the nominal value of the grid angular frequency.

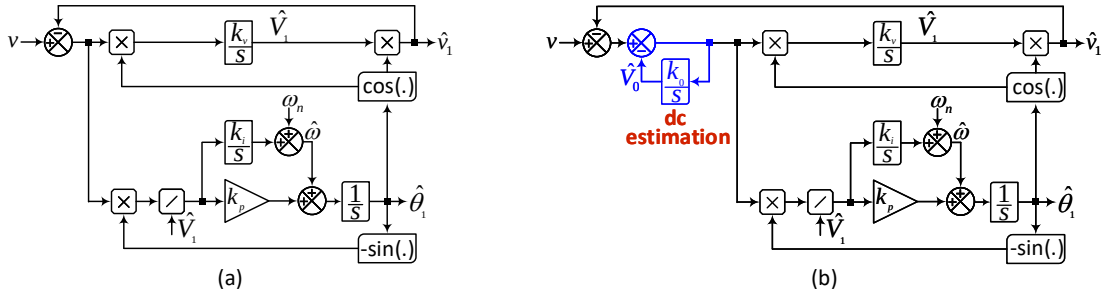

Fig. 2. (a) Conventional EPLL. (b) Modified EPLL (mEPLL). v is the single-phase grid voltage signal, and $\hat{v}_1$ is an estimation of the fundamental component of v. $\hat{V}_0$ is an estimation of the dc component of the signal v.

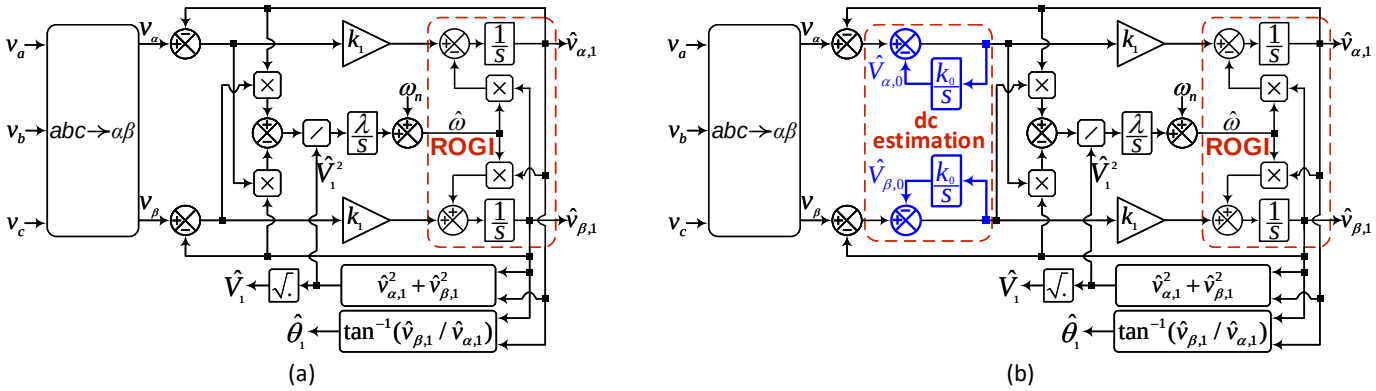

Fig. 3. (a) Conventional ROGI-FLL. (b) Modified ROGI-FLL (mROGI-FLL). k_0, k_1, and λ are the control parameters.

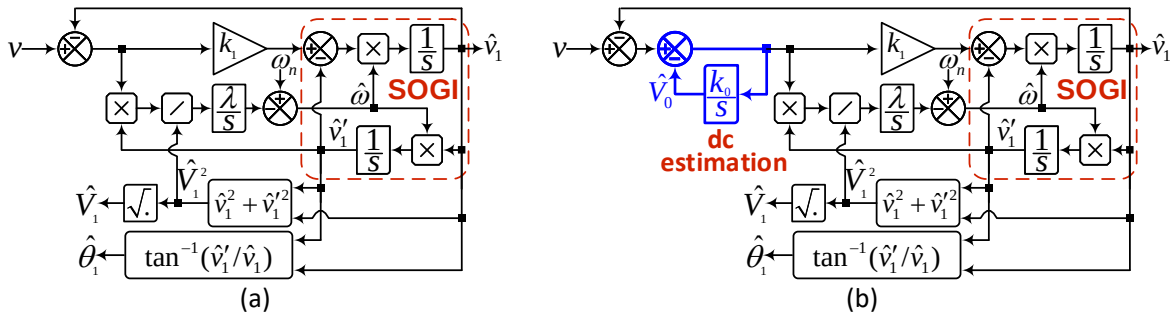

Fig. 4. (a) Conventional SOGI-FLL. (b) Modified SOGI-FLL (mSOGI-FLL). $\hat{v}_1'$ is 90° phase-shifted version of $\hat{v}_1$.

This article has been accepted for publication in a future issue of this journal, but has not been fully edited. Content may change prior to final publication. Citation information: DOI 10.1109/TPEL.2020.3018584, IEEE Transactions on Power Electronics

frequency observer adapts the center frequency of the SOGI to frequency changes.

The conventional SRF-PLL, EPLL, ROGI-FLL, and SOGI-FLL are all highly sensitive to the presence of a dc component in their input. Such a component, which may be caused by different factors such as grid faults, signal conversion process, and measurement devices among others, generates fundamental-frequency oscillatory errors in the output of the above grid synchronization systems and, therefore, may contribute to the dc injection by grid-tied power converters to the power grid [18], [19]. To deal with this challenge, different approaches have been proposed in the literature. The available methods can be divided into two major categories. The first one includes those approaches that only reject the dc component. Using delay signal cancellation operators [2], [19]–[21], BPFs [2], [22]–[24], and notch filters [19] before the input or inside the control loop of the conventional SRF-PLL, EPLL, ROGI-FLL, and SOGI-FLL are examples of these approaches. In the second category, which is the focus of this paper, the available methods provide an estimation of the dc component in addition to rejecting the disturbance effect of this component on the grid synchronization system [1]–[4]. Such methods, therefore, can be beneficial in applications where monitoring and/or compensation of the dc component is required [25], [26].

Adding the dc offset rejection/estimation capability to the conventional SRF-PLL, EPLL, ROGI-FLL, and SOGI-FLL can be carried out in several ways. The simplest possible approach is perhaps including simple dc rejection/estimation loop(s) in the above synchronization systems, which results in the modified SRF-PLL (mSRF-PLL) [Fig. 1(b)], the modified EPLL (mEPLL) [Fig. 2(b)], the modified ROGI-FLL (mROGI-FLL) [Fig. 3(b)], and the modified SOGI-FLL (mSOGI-FLL) [Fig. 4(b)]. This idea, which has been proposed by Karimi Ghartemani *et al.* [18], can be mathematically formulated using the gradient descent method.

Despite the implementation simplicity of the mSRF-PLL, mEPLL, mROGI-FLL, and mSOGI-FLL, no linear model for them has yet been derived. Without such a model, a thorough analysis of these synchronization systems is not possible (at least not easily). The main aim of this paper is to bridge this research gap. To this end, this paper makes the following contributions to the field.

- Through a step-by-step mathematical procedure, a linear time-periodic (LTP) model for the mROGI-FLL is presented. Using this model, the open-loop harmonic transfer function (HTF) of the mROGI-FLL is obtained, the effects of the control parameters on its stability are briefly discussed, and its stability region is determined.
- It is shown how using the derived LTP model, a linear time-invariant (LTI) model for the mROGI-FLL can be obtained.
- Using the obtained linear models and some numerical results, the dynamic couplings between the amplitude and phase/frequency variables of the mROGI-FLL is discussed, and a simple yet efficient solution for decoupling these variables is proposed.

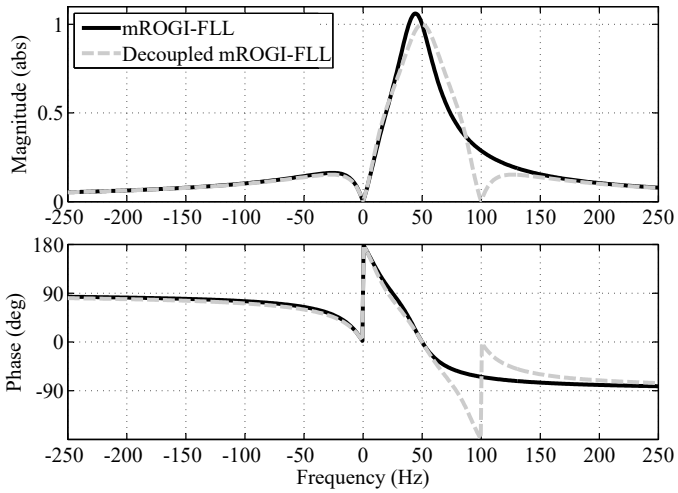

Fig. 5. Frequency response of the input-output transfer functions of the mROGI-FLL and the decoupled mROGI-FLL. Parameters: $k_0 = k_1 = k_2 = 100$ rad/s and $\hat{\omega} = \omega_n = 2\pi 50$ rad/s.

- The relationship of the mROGI-FLL and mSRF-PLL is briefly investigated.
- Finally, an LTP model for the mSOGI-FLL is presented, and the relationship between the mSOGI-FLL and mEPLL is discussed.

II. Modified ROGI-FLL (mROGI-FLL)

A. LTP Modeling

1) Assumptions: For obtaining the LTP model of the mROGI-FLL, it is assumed that the three-phase grid voltage of the mROGI-FLL contains only the FFPS component and a dc component, as expressed in (1), in which V_1 and θ_1 are the amplitude and phase angle of the FFPS component, respectively, and $V_{a,0}$, $V_{b,0}$ and $V_{c,0}$ are the dc component in three phases.

$$\begin{aligned} v_a(t) &= V_1 \cos(\theta_1) + V_{a,0} \\ v_b(t) &= V_1 \cos(\theta_1 - 2\pi/3) + V_{b,0} \\ v_a(t) &= V_1 \cos(\theta_1 + 2\pi/3) + V_{c,0} \end{aligned} \tag{1}$$

Transferring (1) to the $\alpha\beta$ frame yields

$$\begin{aligned} v_\alpha(t) &= V_1 \cos(\theta_1) + V_{\alpha,0} \\ v_\beta(t) &= V_1 \sin(\theta_1) + V_{\beta,0} \end{aligned} \tag{2}$$

where $V_{\alpha,0} = \frac{2}{3}\left(V_{a,0} - 0.5V_{b,0} - 0.5V_{c,0}\right)$ and $V_{\beta,0} = \frac{1}{\sqrt{3}}\left(V_{b,0} - V_{c,0}\right)$.

If we assume that $\hat{\omega}$ is a constant, the transfer function between the input signals v_α and v_β and the output signals $\hat{v}_{\alpha,1}$ and $\hat{v}_{\beta,1}$ in Fig. 3(b) can be obtained as

$$G(s) = \frac{\hat{v}_{\alpha,1}(s) + j\hat{v}_{\beta,1}(s)}{v_\alpha(s) + jv_\beta(s)} = \frac{k_1 s}{s^2 + (k_0 + k_1 - j\hat{\omega})s - jk_0\hat{\omega}}. \tag{3}$$

The solid lines in Fig. 5 show the frequency response of this transfer function. It is observed that it is a complex band-pass/notch filter that passes the FFPS component and blocks the dc component. It means that the output signals $\hat{v}_{\alpha,1}$ and $\hat{v}_{\beta,1}$ in the mROGI-FLL are estimations of the

FFPS component of the input signals v_α and v_β, respectively. Therefore, by considering (2), the output signals $\hat{v}_{\alpha,1}$ and $\hat{v}_{\beta,1}$ can be expressed as

$$\hat{v}_{\alpha,1}(t) = \hat{V}_1 \cos(\hat{\theta}_1), \quad \hat{v}_{\beta,1}(t) = \hat{V}_1 \sin(\hat{\theta}_1) \tag{4}$$

where $\hat{V}_1$ and $\hat{\theta}_1$ are estimations of V_1 and θ_1 in (2), respectively. By following a similar procedure, it can be shown that the output signals $\hat{V}_{\alpha,0}$ and $\hat{V}_{\beta,0}$ in Fig. 3(b) are estimations of the dc component of the input signals v_α and v_β in (2).

The mROGI-FLL is also assumed to be working under a quasi-locked condition, which is corresponding to $\hat{V}_{\alpha,0} \approx V_{\alpha,0}$, $\hat{V}_{\beta,0} \approx V_{\beta,0}$, $\hat{V}_1 \approx V_1$, $\hat{\theta}_1 \approx \theta_1$, and $\hat{\omega} \approx \omega$. All these parameters are also defined as a nominal value (indicated by the subscript n) plus a small perturbation (indicated by Δ), as follows

$$\begin{array}{ll} \hat{V}_{\alpha,0} = V_{n,0} + \Delta\hat{V}_{\alpha,0}, & V_{\alpha,0} = V_{n,0} + \Delta V_{\alpha,0} \\ \hat{V}_{\beta,0} = V_{n,0} + \Delta\hat{V}_{\beta,0}, & V_{\beta,0} = V_{n,0} + \Delta V_{\beta,0} \\ \hat{V}_1 = V_{n,1} + \Delta\hat{V}_1, & V_1 = V_{n,1} + \Delta V_1 \\ \hat{\theta}_1 = \theta_{n,1} + \Delta\hat{\theta}_1, & \theta_1 = \theta_{n,1} + \Delta\theta_1 \\ \hat{\omega} = \omega_n + \Delta\hat{\omega}, & \omega = \omega_n + \Delta\omega. \end{array} \tag{5}$$

Throughout this paper $V_{n,1} = 1$ p.u., $\omega_n = 2\pi 50$ rad/s, $\theta_{n,1} = \int \omega_n dt = \omega_n t$ are considered.

2) Governing Nonlinear Differential Equations: From Fig. 3(b), the estimated dc components and the estimated angular frequency, phase angle, and amplitude of the FFPS component can be expressed as

$$\hat{V}_{\alpha,0} = k_0 \int (v_\alpha - \hat{v}_{\alpha,1} - \hat{V}_{\alpha,0}) dt \tag{6a}$$

$$\hat{V}_{\beta,0} = k_0 \int (v_\beta - \hat{v}_{\beta,1} - \hat{V}_{\beta,0}) dt \tag{6b}$$

$$\hat{\omega} = \omega_n + \lambda \int \frac{(v_\beta - \hat{V}_{\beta,0})\hat{v}_{\alpha,1} - (v_\alpha - \hat{V}_{\alpha,0})\hat{v}_{\beta,1}}{\hat{V}_1^2} dt \tag{6c}$$

$$\hat{\theta}_1 = \tan^{-1}\left(\frac{\hat{v}_{\beta,1}}{\hat{v}_{\alpha,1}}\right) \tag{6d}$$

$$\hat{V}_1 = \sqrt{\hat{v}_{\alpha,1}^2 + \hat{v}_{\beta,1}^2}. \tag{6e}$$

The time derivative of (6) is

$$\frac{d\hat{V}_{\alpha,0}}{dt} = k_0(v_\alpha - \hat{v}_{\alpha,1} - \hat{V}_{\alpha,0}) \tag{7a}$$

$$\frac{d\hat{V}_{\beta,0}}{dt} = k_0(v_\beta - \hat{v}_{\beta,1} - \hat{V}_{\beta,0}) \tag{7b}$$

$$\frac{d\hat{\omega}}{dt} = \lambda \frac{(v_\beta - \hat{V}_{\beta,0})\hat{v}_{\alpha,1} - (v_\alpha - \hat{V}_{\alpha,0})\hat{v}_{\beta,1}}{\hat{V}_1^2} \tag{7c}$$

$$\frac{d\hat{\theta}_1}{dt} = \frac{\hat{v}_{\alpha,1}\frac{d\hat{v}_{\beta,1}}{dt} - \hat{v}_{\beta,1}\frac{d\hat{v}_{\alpha,1}}{dt}}{\hat{V}_1^2} \tag{7d}$$

$$\frac{d\hat{V}_1}{dt} = \frac{\hat{v}_{\alpha,1}\frac{d\hat{v}_{\alpha,1}}{dt} + \hat{v}_{\beta,1}\frac{d\hat{v}_{\beta,1}}{dt}}{\hat{V}_1} \tag{7e}$$

where $\frac{d\hat{v}_{\alpha,1}}{dt}$ and $\frac{d\hat{v}_{\beta,1}}{dt}$, according to Fig. 3(b), are equal to

$$\frac{d\hat{v}_{\alpha,1}}{dt} = -\hat{\omega}\hat{v}_{\beta,1} + k_1(v_\alpha - \hat{v}_{\alpha,1} - \hat{V}_{\alpha,0}) \tag{8a}$$

$$\frac{d\hat{v}_{\beta,1}}{dt} = +\hat{\omega}\hat{v}_{\alpha,1} + k_1(v_\beta - \hat{v}_{\beta,1} - \hat{V}_{\beta,0}). \tag{8b}$$

Substituting (8) into (7d) and (7e) results in

$$\frac{d\hat{\theta}_1}{dt} = \frac{\hat{\omega}[\hat{v}_{\alpha,1}^2 + \hat{v}_{\beta,1}^2] + k_1 \overbrace{[(v_\beta - \hat{V}_{\beta,0})\hat{v}_{\alpha,1} - (v_\alpha - \hat{V}_{\alpha,0})\hat{v}_{\beta,1}]}^{\frac{\hat{V}_1^2}{\lambda}\frac{d\hat{\omega}}{dt}}}{\hat{V}_1^2} \tag{9a}$$

$$\frac{d\hat{V}_1}{dt} = k_1 \frac{\hat{v}_{\alpha,1}(v_\alpha - \hat{v}_{\alpha,1} - \hat{V}_{\alpha,0}) + \hat{v}_{\beta,1}(v_\beta - \hat{v}_{\beta,1} - \hat{V}_{\beta,0})}{\hat{V}_1}. \tag{9b}$$

Equations (7a)-(7c) and (9) are a set of nonlinear differential equations that describe the governing dynamics of the mROGI-FLL. To obtain a linear model, these equations are linearized in the next section.

3) Linearization: Substituting (2) and (4) into (7a)-(7c) and (9) gives

$$\frac{d\hat{V}_{\alpha,0}}{dt} = k_0\left[V_1\cos(\theta_1) + V_{\alpha,0} - \hat{V}_1\cos(\hat{\theta}_1) - \hat{V}_{\alpha,0}\right] \tag{10a}$$

$$\frac{d\hat{V}_{\beta,0}}{dt} = k_0\left[V_1\sin(\theta_1) + V_{\beta,0} - \hat{V}_1\sin(\hat{\theta}_1) - \hat{V}_{\beta,0}\right] \tag{10b}$$

$$\frac{d\hat{\omega}}{dt} = \frac{\lambda}{\hat{V}_1}\Big[\, V_1\sin(\theta_1 - \hat{\theta}_1) + (V_{\beta,0} - \hat{V}_{\beta,0})\cos(\hat{\theta}_1) - (V_{\alpha,0} - \hat{V}_{\alpha,0})\sin(\hat{\theta}_1)\,\Big] \tag{10c}$$

$$\frac{d\hat{\theta}_1}{dt} = \hat{\omega} + \frac{k_1}{\lambda}\frac{d\hat{\omega}}{dt} \tag{10d}$$

$$\frac{d\hat{V}_1}{dt} = k_1\Big[\, V_1\cos(\theta_1 - \hat{\theta}_1) - \hat{V}_1 + (V_{\alpha,0} - \hat{V}_{\alpha,0})\cos(\hat{\theta}_1) + (V_{\beta,0} - \hat{V}_{\beta,0})\sin(\hat{\theta}_1)\,\Big]. \tag{10e}$$

Considering the definitions (5) and using trigonometric identities, (10) can be approximated by (11) on the next page, which is a set of LTP differential equations. Using (11), the linear model of the mROGI-FLL, which is an LTP model, can be obtained, as shown in Fig. 6.

B. Stability Analysis

1) Harmonic Transfer Function (HTF): The obtained linear model for the mROGI-FLL, as mentioned before, has an LTP nature. It implies that there are dynamic couplings among different frequency components and, therefore, the concept of transfer function will be elusive. To take into account these couplings, the HTF method needs to be adopted for the stability analysis [27]–[29]. Mathematically speaking, the HTF is the translation of an LTP system to an LTI system with an infinite dimension. In this way, the theory of multivariable LTI feedback control can be applied for the analysis. In what follows, the open-loop HTF of the mROGI-FLL is obtained.

Considering the fact that $\mathcal{L}[\cos(\omega_n t)E(t)] = \frac{1}{2}E(s + j\omega_n) + \frac{1}{2}E(s - j\omega_n)$ and $\mathcal{L}[\sin(\omega_n t)E(t)] = \frac{j}{2}E(s + j\omega_n) - \frac{j}{2}E(s - j\omega_n)$, where $\mathcal{L}$ denotes the Laplace transform and $E(s) = \mathcal{L}[E(t)]$, the output signals $\Delta\hat{V}_{\alpha,0}$, $\Delta\hat{V}_{\beta,0}$, $\Delta\hat{\theta}_1$, and $\Delta\hat{V}_1$ in Fig. 6 can be expressed in the Laplace domain as (12). By defining $H(s) = \frac{s + \overbrace{\lambda/k_1}^{\omega_z}}{s^2}$, $G(s) = \frac{1}{s}$, $s_m = s + jm\omega_n$ ($m \in Z$), and $k_0 = rk_1$, and substituting s by s_m in (12), it can be rewritten as (13). In the matrix form, (13) is corresponding

This article has been accepted for publication in a future issue of this journal, but has not been fully edited. Content may change prior to final publication. Citation information: DOI 10.1109/TPEL.2020.3018584, IEEE Transactions on Power Electronics

$$\frac{d\Delta\hat{V}_{\alpha,0}}{dt} = k_0\left[(V_{n,1}+\Delta V_1)\cos(\theta_{n,1}+\Delta\theta_1) - (V_{n,1}+\Delta\hat{V}_1)\cos(\theta_{n,1}+\Delta\hat{\theta}_1) + \Delta V_{\alpha,0} - \Delta\hat{V}_{\alpha,0}\right]$$

$$= k_0\Bigg[V_{n,1}\cos(\theta_{n,1})\overbrace{\left\{\cos(\Delta\theta_1)-\cos(\Delta\hat{\theta}_1)\right\}}^{\approx 0} - V_{n,1}\sin(\theta_{n,1})\overbrace{\left\{\sin(\Delta\theta_1)-\sin(\Delta\hat{\theta}_1)\right\}}^{\approx\Delta\theta_1-\Delta\hat{\theta}_1} + \Delta V_{\alpha,0} - \Delta\hat{V}_{\alpha,0}$$

$$+\cos(\theta_{n,1})\overbrace{\left\{\Delta V_1\cos(\Delta\theta_1)-\Delta\hat{V}_1\cos(\Delta\hat{\theta}_1)\right\}}^{\approx\Delta V_1-\Delta\hat{V}_1} - \sin(\theta_{n,1})\overbrace{\left\{\Delta V_1\sin(\Delta\theta_1)-\Delta\hat{V}_1\sin(\Delta\hat{\theta}_1)\right\}}^{\approx 0}\Bigg]$$

$$\approx k_0\left[(\Delta V_1-\Delta\hat{V}_1)\cos(\theta_{n,1}) - V_{n,1}(\Delta\theta_1-\Delta\hat{\theta}_1)\sin(\theta_{n,1}) + \Delta V_{\alpha,0} - \Delta\hat{V}_{\alpha,0}\right] \tag{11a}$$

$$\frac{d\Delta\hat{V}_{\beta,0}}{dt} = k_0\left[(V_{n,1}+\Delta V_1)\sin(\theta_{n,1}+\Delta\theta_1) - (V_{n,1}+\Delta\hat{V}_1)\sin(\theta_{n,1}+\Delta\hat{\theta}_1) + \Delta V_{\beta,0} - \Delta\hat{V}_{\beta,0}\right]$$

$$= k_0\Bigg[V_{n,1}\sin(\theta_{n,1})\overbrace{\left\{\cos(\Delta\theta_1)-\cos(\Delta\hat{\theta}_1)\right\}}^{\approx 0} + V_{n,1}\cos(\theta_{n,1})\overbrace{\left\{\sin(\Delta\theta_1)-\sin(\Delta\hat{\theta}_1)\right\}}^{\approx\Delta\theta_1-\Delta\hat{\theta}_1} + \Delta V_{\beta,0} - \Delta\hat{V}_{\beta,0}$$

$$+\sin(\theta_{n,1})\overbrace{\left\{\Delta V_1\cos(\Delta\theta_1)-\Delta\hat{V}_1\cos(\Delta\hat{\theta}_1)\right\}}^{\approx\Delta V_1-\Delta\hat{V}_1} + \cos(\theta_{n,1})\overbrace{\left\{\Delta V_1\sin(\Delta\theta_1)-\Delta\hat{V}_1\sin(\Delta\hat{\theta}_1)\right\}}^{\approx 0}\Bigg]$$

$$\approx k_0\left[(\Delta V_1-\Delta\hat{V}_1)\sin(\theta_{n,1}) + V_{n,1}(\Delta\theta_1-\Delta\hat{\theta}_1)\cos(\theta_{n,1}) + \Delta V_{\beta,0} - \Delta\hat{V}_{\beta,0}\right] \tag{11b}$$

$$\frac{d\Delta\hat{\omega}}{dt} = \overbrace{\frac{\lambda}{V_{n,1}+\Delta\hat{V}_1}}^{\approx\frac{\lambda}{V_{n,1}}\left(1-\frac{\Delta\hat{V}_1}{V_{n,1}}\right)}\Bigg[(V_{n,1}+\Delta V_1)\overbrace{\sin(\Delta\theta_1-\Delta\hat{\theta}_1)}^{\approx\Delta\theta_1-\Delta\hat{\theta}_1} + (\Delta V_{\beta,0}-\Delta\hat{V}_{\beta,0})\cos(\theta_{n,1}+\Delta\hat{\theta}_1)$$

$$-(\Delta V_{\alpha,0}-\Delta\hat{V}_{\alpha,0})\sin(\theta_{n,1}+\Delta\hat{\theta}_1)\Bigg]$$

$$\approx \frac{\lambda}{V_{n,1}}\left(1-\frac{\Delta\hat{V}_1}{V_{n,1}}\right)\Bigg[V_{n,1}(\Delta\theta_1-\Delta\hat{\theta}_1) + \overbrace{(\Delta V_{\beta,0}-\Delta\hat{V}_{\beta,0})\cos(\Delta\hat{\theta}_1)}^{\approx(\Delta V_{\beta,0}-\Delta\hat{V}_{\beta,0})}\cos(\theta_{n,1}) - \overbrace{(\Delta V_{\beta,0}-\Delta\hat{V}_{\beta,0})\sin(\Delta\hat{\theta}_1)}^{\approx 0}\sin(\theta_{n,1})$$

$$-\overbrace{(\Delta V_{\alpha,0}-\Delta\hat{V}_{\alpha,0})\cos(\Delta\hat{\theta}_1)}^{\approx(\Delta V_{\alpha,0}-\Delta\hat{V}_{\alpha,0})}\sin(\theta_{n,1}) - \overbrace{(\Delta V_{\alpha,0}-\Delta\hat{V}_{\alpha,0})\sin(\Delta\hat{\theta}_1)}^{\approx 0}\cos(\theta_{n,1})\Bigg]$$

$$\approx \frac{\lambda}{V_{n,1}}\left[V_{n,1}(\Delta\theta_1-\Delta\hat{\theta}_1) + (\Delta V_{\beta,0}-\Delta\hat{V}_{\beta,0})\cos(\theta_{n,1}) - (\Delta V_{\alpha,0}-\Delta\hat{V}_{\alpha,0})\sin(\theta_{n,1})\right] \tag{11c}$$

$$\frac{d\Delta\hat{\theta}_1}{dt} = \Delta\hat{\omega} + \frac{k_1}{\lambda}\frac{d\Delta\hat{\omega}}{dt} \tag{11d}$$

$$\frac{d\Delta\hat{V}_1}{dt} = k_1\Bigg[\overbrace{(V_{n,1}+\Delta V_1)\cos(\Delta\theta_1-\Delta\hat{\theta}_1)-(V_{n,1}+\Delta\hat{V}_1)}^{\approx\Delta V_1-\Delta\hat{V}_1} + (\Delta V_{\alpha,0}-\Delta\hat{V}_{\alpha,0})\cos(\theta_{n,1}+\Delta\hat{\theta}_1)$$

$$+(\Delta V_{\beta,0}-\Delta\hat{V}_{\beta,0})\sin(\theta_{n,1}+\Delta\hat{\theta}_1)\Bigg]$$

$$\approx k_1\left[(\Delta V_1-\Delta\hat{V}_1) + (\Delta V_{\alpha,0}-\Delta\hat{V}_{\alpha,0})\cos(\theta_{n,1}) + (\Delta V_{\beta,0}-\Delta\hat{V}_{\beta,0})\sin(\theta_{n,1})\right] \tag{11e}$$

This article has been accepted for publication in a future issue of this journal, but has not been fully edited. Content may change prior to final publication. Citation information: DOI 10.1109/TPEL.2020.3018584, IEEE Transactions on Power Electronics

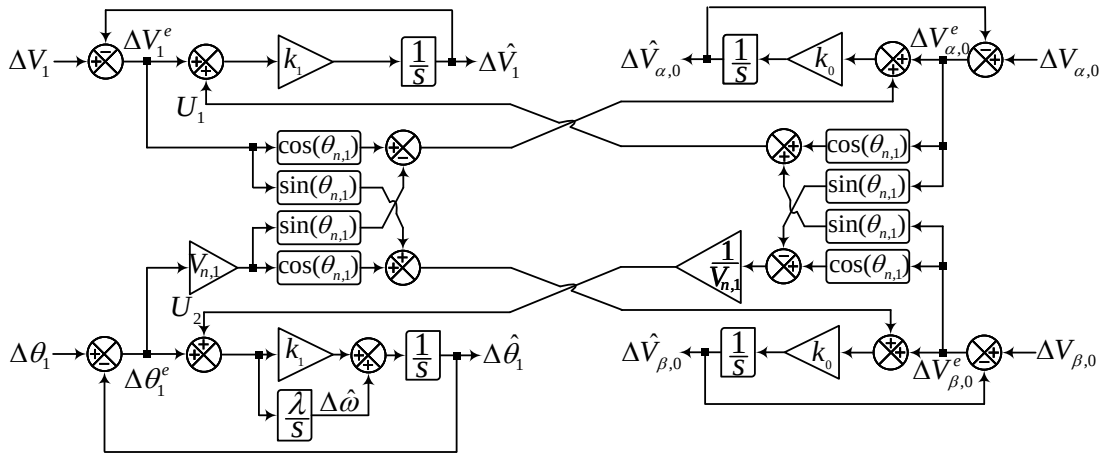

Fig. 6. LTP model of the mROGI-FLL. It will be proved later that this LTP model is also valid for the mSRF-PLL. The only point is that the control parameters in this model need to be replaced by those of the mSRF-PLL. To be more exact, the gain k_1 in the upper and lower control loops of this model needs to be replaced by k_v and k_p, respectively, and the gain λ needs to be replaced by k_i.

to (14) at the bottom of the next page, which is the open-loop HTF of the mROGI-FLL. Fig. 7(a) shows the block diagram representation of (14).

Notice that (14) has an infinite dimension. Therefore, its truncated version needs to be considered for the analysis.

2) Stability Region: The mROGI-FLL stability can be analyzed using the generalized Nyquist stability criterion for the LTP systems [27]. According to this criterion, the LTP feedback control system in Fig. 7(a) is stable if the point $-1/k_1$ is encircled N_p times in an anticlockwise direction by the eigenloci[2] of $G_{\mathcal{HTF}}(s)$ for s belonging to the counter shown in Fig. 7(b), where N_p is the number of open-loop poles of $G_{\mathcal{HTF}}(s)$ in the right-half plane.

Fig. 8 shows the LTP Nyquist plots of the HTF $G_{\mathcal{HTF}}(s)$ for different set of control parameters. According to the generalized Nyquist stability criterion, the stability range of the control gain k_1 in each plot is as follows.

- Fig. 8(a): $-\infty < -\frac{1}{k_1} < -5.655e-4$ or $0 < k_1 < 1768.3$.
- Fig. 8(b): $-\infty < -\frac{1}{k_1} < -2.0631e-3$ or $0 < k_1 < 484.7$.
- Fig. 8(c): $-\infty < -\frac{1}{k_1} < -9.948e-4$ or $0 < k_1 < 1005.2$.
- Fig. 8(d): $-\infty < -\frac{1}{k_1} < -3.2988e-3$ or $0 < k_1 < 303.1$.

The above observations indicate that increasing the ratio $r = k_0/k_1$ and/or $\omega_z = \lambda/k_1$ reduces the stability range of the control gain k_1. This fact can be better visualized in Fig. 9, which shows the stability regions of the mROGI-FLL for two different values of r ($r = 0.5$ in the left plot and $r = 1$ in the right plot). A noticeable reduction in the stability region of the mROGI-FLL by increasing the ratio r is observed. Notice that $r = 0$, which is corresponding to $k_0 = 0$ and, therefore,

[2]The eigenloci of $G_{\mathcal{HTF}}(s)$ are the closed curves generated by the eigenvalues of $G_{\mathcal{HTF}}(s)$ in the complex plane.

$$\Delta\hat{V}_{\alpha,0}(s) \approx \frac{k_0}{2s}\left[jV_{n,1}\Delta\theta_1^e(s-j\omega_n) + \Delta V_1^e(s-j\omega_n) + 2\Delta V_{\alpha,0}^e(s) - jV_{n,1}\Delta\theta_1^e(s+j\omega_n) + \Delta V_1^e(s+j\omega_n)\right] \tag{12a}$$

$$\Delta\hat{V}_{\beta,0}(s) \approx \frac{k_0}{2s}\left[V_{n,1}\Delta\theta_1^e(s-j\omega_n) - j\Delta V_1^e(s-j\omega_n) + 2\Delta V_{\beta,0}^e(s) + V_{n,1}\Delta\theta_1^e(s+j\omega_n) + j\Delta V_1^e(s+j\omega_n)\right] \tag{12b}$$

$$\Delta\hat{\theta}_1(s) \approx \frac{k_1 s+\lambda}{2V_{n,1}s^2}\left[j\Delta V_{\alpha,0}^e(s-j\omega_n) + \Delta V_{\beta,0}^e(s-j\omega_n) + 2V_{n,1}\Delta\theta_1^e(s) - j\Delta V_{\alpha,0}^e(s+j\omega_n) + \Delta V_{\beta,0}^e(s+j\omega_n)\right] \tag{12c}$$

$$\Delta\hat{V}_1(s) \approx \frac{k_1}{2s}\left[\Delta V_{\alpha,0}^e(s-j\omega_n) - j\Delta V_{\beta,0}^e(s-j\omega_n) + 2\Delta V_1^e(s) + \Delta V_{\alpha,0}^e(s+j\omega_n) + j\Delta V_{\beta,0}^e(s+j\omega_n)\right]. \tag{12d}$$

$$\Delta\hat{V}_{\alpha,0}(s_m) \approx \frac{rk_1G(s_m)}{2}\left[jV_{n,1}\Delta\theta_1^e(s_{m-1}) + \Delta V_1^e(s_{m-1}) + 2\Delta V_{\alpha,0}^e(s_m) - jV_{n,1}\Delta\theta_1^e(s_{m+1}) + \Delta V_1^e(s_{m+1})\right] \tag{13a}$$

$$\Delta\hat{V}_{\beta,0}(s_m) \approx \frac{rk_1G(s_m)}{2}\left[V_{n,1}\Delta\theta_1^e(s_{m-1}) - j\Delta V_1^e(s_{m-1}) + 2\Delta V_{\beta,0}^e(s_m) + V_{n,1}\Delta\theta_1^e(s_{m+1}) + j\Delta V_1^e(s_{m+1})\right] \tag{13b}$$

$$\Delta\hat{\theta}_1(s_m) \approx \frac{k_1H(s_m)}{2V_{n,1}}\left[j\Delta V_{\alpha,0}^e(s_{m-1}) + \Delta V_{\beta,0}^e(s_{m-1}) + 2V_{n,1}\Delta\theta_1^e(s_m) - j\Delta V_{\alpha,0}^e(s_{m+1}) + \Delta V_{\beta,0}^e(s_{m+1})\right] \tag{13c}$$

$$\Delta\hat{V}_1(s_m) \approx \frac{k_1G(s_m)}{2}\left[\Delta V_{\alpha,0}^e(s_{m-1}) - j\Delta V_{\beta,0}^e(s_{m-1}) + 2\Delta V_1^e(s_m) + \Delta V_{\alpha,0}^e(s_{m+1}) + j\Delta V_{\beta,0}^e(s_{m+1})\right]. \tag{13d}$$

This article has been accepted for publication in a future issue of this journal, but has not been fully edited. Content may change prior to final publication. Citation information: DOI 10.1109/TPEL.2020.3018584, IEEE Transactions on Power Electronics

removing the dc rejection/estimation loop of the mROGI-FLL, makes the region of its stability of infinite size. It is reasonable because, without its dc rejection/estimation loop, the mROGI-FLL turns to a simple ROGI-FLL, which is unconditionally stable from the small-signal point of view.

C. LTI modeling

Based on the LTP model in Fig. 6, an LTI model may also be obtained for the mROGI-FLL, which further facilitates its analysis. Obtaining such a model requires to assume that the perturbation terms $\Delta V_{\alpha,0}$ and $\Delta V_{\beta,0}$ in the LTP model of the mROGI-FLL are equal to zero. It implies that the resulting LTI model will not be able to predict any transient in the mROGI-FLL output caused by the change of dc component in its input. In what follows, the procedure for obtaining the LTI model of the mROGI-FLL from its LTP model is explained.

By considering $\Delta V_{\alpha,0} = 0$ and $\Delta V_{\beta,0} = 0$ in Fig. 6, the signals U_1, U_2, $\Delta\hat{V}_{\alpha,0}$, and $\Delta\hat{V}_{\beta,0}$ in this figure can be expressed in the time domain as

$$\begin{aligned} U_1(t) &= -\cos(\theta_{n,1})\Delta\hat{V}_{\alpha,0}(t) - \sin(\theta_{n,1})\Delta\hat{V}_{\beta,0}(t) \\ U_2(t) &= \tfrac{\sin(\theta_{n,1})}{V_{n,1}}\Delta\hat{V}_{\alpha,0}(t) - \tfrac{\cos(\theta_{n,1})}{V_{n,1}}\Delta\hat{V}_{\beta,0}(t) \end{aligned} \tag{15}$$

$$\begin{aligned} \Delta\hat{V}_{\alpha,0}(t) &= L(t) * \{\cos(\theta_{n,1})\Delta V_1^e(t) - V_{n,1}\sin(\theta_{n,1})\Delta\theta_1^e(t)\} \\ \Delta\hat{V}_{\beta,0}(t) &= L(t) * \{\sin(\theta_{n,1})\Delta V_1^e(t) + V_{n,1}\cos(\theta_{n,1})\Delta\theta_1^e(t)\} \end{aligned} \tag{16}$$

where $L(t)$ is the inverse Laplace of $L(s) = \frac{k_0}{s+k_0}$ and $*$ denotes the convolution product.

Taking the Laplace transform of (15) and (16) results in

$$\begin{aligned} U_1(s) = -\frac{1}{2}\Big[&\Delta\hat{V}_{\alpha,0}(s-j\omega_n) + \Delta\hat{V}_{\alpha,0}(s+j\omega_n) \\ &+ j\Delta\hat{V}_{\beta,0}(s+j\omega_n) - j\Delta\hat{V}_{\beta,0}(s-j\omega_n)\Big] \end{aligned} \tag{17a}$$

$$\begin{aligned} U_2(s) = -\frac{1}{2V_{n,1}}\Big[&j\Delta\hat{V}_{\alpha,0}(s-j\omega_n) - j\Delta\hat{V}_{\alpha,0}(s+j\omega_n) \\ &+ \Delta\hat{V}_{\beta,0}(s-j\omega_n) + \Delta\hat{V}_{\beta,0}(s+j\omega_n)\Big] \end{aligned} \tag{17b}$$

$$\underbrace{\begin{bmatrix} \vdots \\ \Delta\hat{V}_{\alpha,0}(s_{-1}) \\ \Delta\hat{V}_{\beta,0}(s_{-1}) \\ \Delta\hat{\theta}_1(s_{-1}) \\ \Delta\hat{V}_1(s_{-1}) \\ \Delta\hat{V}_{\alpha,0}(s_0) \\ \Delta\hat{V}_{\beta,0}(s_0) \\ \Delta\hat{\theta}_1(s_0) \\ \Delta\hat{V}_1(s_0) \\ \Delta\hat{V}_{\alpha,0}(s_{+1}) \\ \Delta\hat{V}_{\beta,0}(s_{+1}) \\ \Delta\hat{\theta}_1(s_{+1}) \\ \Delta\hat{V}_1(s_{+1}) \\ \vdots \end{bmatrix}}_{Y} = k_1 \begin{bmatrix} \ddots & \vdots & \vdots & \vdots & \vdots & \vdots & \vdots \\ \cdots & rG(s_{-1}) & 0 & 0 & 0 & 0 & 0 \\ \cdots & 0 & rG(s_{-1}) & 0 & 0 & 0 & 0 \\ \cdots & 0 & 0 & H(s_{-1}) & 0 & -\frac{jH(s_{-1})}{2V_{n,1}} & \frac{H(s_{-1})}{2V_{n,1}} \\ \cdots & 0 & 0 & 0 & G(s_{-1}) & \frac{G(s_{-1})}{2} & \frac{jG(s_{-1})}{2} \\ \cdots & 0 & 0 & \frac{jV_{n,1}rG(s_0)}{2} & \frac{rG(s_0)}{2} & rG(s_0) & 0 \\ \cdots & 0 & 0 & \frac{V_{n,1}rG(s_0)}{2} & -\frac{jrG(s_0)}{2} & 0 & rG(s_0) \\ \cdots & \frac{jH(s_0)}{2V_{n,1}} & \frac{H(s_0)}{2V_{n,1}} & 0 & 0 & 0 & 0 \\ \cdots & \frac{G(s_0)}{2} & -\frac{jG(s_0)}{2} & 0 & 0 & 0 & 0 \\ \cdots & 0 & 0 & 0 & 0 & 0 & 0 \\ \cdots & 0 & 0 & 0 & 0 & 0 & 0 \\ \cdots & 0 & 0 & 0 & 0 & \frac{jH(s_{+1})}{2V_{n,1}} & \frac{H(s_{+1})}{2V_{n,1}} \\ \cdots & 0 & 0 & 0 & 0 & \frac{G(s_{+1})}{2} & -\frac{jG(s_{+1})}{2} \\ \iddots & \vdots & \vdots & \vdots & \vdots & \vdots & \vdots \end{bmatrix}$$

$$\begin{bmatrix} \vdots & \vdots & \vdots & \vdots & \vdots & \vdots & \iddots \\ -\frac{jV_{n,1}rG(s_{-1})}{2} & \frac{rG(s_{-1})}{2} & 0 & 0 & 0 & 0 & \cdots \\ \frac{V_{n,1}rG(s_{-1})}{2} & \frac{jrG(s_{-1})}{2} & 0 & 0 & 0 & 0 & \cdots \\ 0 & 0 & 0 & 0 & 0 & 0 & \cdots \\ 0 & 0 & 0 & 0 & 0 & 0 & \cdots \\ 0 & 0 & 0 & 0 & -\frac{jV_{n,1}rG(s_0)}{2} & \frac{rG(s_0)}{2} & \cdots \\ 0 & 0 & 0 & 0 & \frac{V_{n,1}rG(s_0)}{2} & \frac{jrG(s_0)}{2} & \cdots \\ H(s_0) & 0 & -\frac{jH(s_0)}{2V_{n,1}} & \frac{H(s_0)}{2V_{n,1}} & 0 & 0 & \cdots \\ 0 & G(s_0) & \frac{G(s_0)}{2} & \frac{jG(s_0)}{2} & 0 & 0 & \cdots \\ \frac{jV_{n,1}rG(s_{+1})}{2} & \frac{rG(s_{+1})}{2} & rG(s_{+1}) & 0 & 0 & 0 & \cdots \\ \frac{V_{n,1}rG(s_{+1})}{2} & -\frac{jrG(s_{+1})}{2} & 0 & rG(s_{+1}) & 0 & 0 & \cdots \\ 0 & 0 & 0 & 0 & H(s_{+1}) & 0 & \cdots \\ 0 & 0 & 0 & 0 & 0 & G(s_{+1}) & \cdots \\ \vdots & \vdots & \vdots & \vdots & \vdots & \vdots & \ddots \end{bmatrix} \underbrace{\begin{bmatrix} \vdots \\ \Delta V_{\alpha,0}^e(s_{-1}) \\ \Delta V_{\beta,0}^e(s_{-1}) \\ \Delta\theta_1^e(s_{-1}) \\ \Delta V_1^e(s_{-1}) \\ \Delta V_{\alpha,0}^e(s_0) \\ \Delta V_{\beta,0}^e(s_0) \\ \Delta\theta_1^e(s_0) \\ \Delta V_1^e(s_0) \\ \Delta V_{\alpha,0}^e(s_{+1}) \\ \Delta V_{\beta,0}^e(s_{+1}) \\ \Delta\theta_1^e(s_{+1}) \\ \Delta V_1^e(s_{+1}) \\ \vdots \end{bmatrix}}_{E} \tag{14}$$

This article has been accepted for publication in a future issue of this journal, but has not been fully edited. Content may change prior to final publication. Citation information: DOI 10.1109/TPEL.2020.3018584, IEEE Transactions on Power Electronics

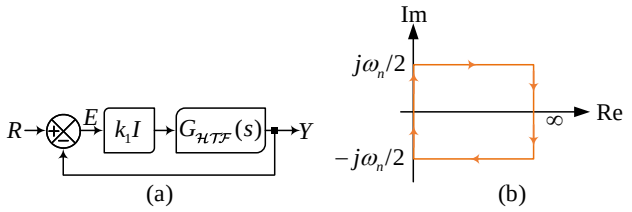

Fig. 7. (a) LTP feedback control system described by the open-loop HTF in (14). (b) LTP Nyquist counter.

$$\Delta\hat{V}_{\alpha,0}(s)= \frac{L(s)}{2}\left[\Delta V_1^e(s-j\omega_n)+\Delta V_1^e(s+j\omega_n)\right. \\ \left.+jV_{n,1}\Delta\theta_1^e(s-j\omega_n)-jV_{n,1}\Delta\theta_1^e(s+j\omega_n)\right] \quad (18a)$$

$$\Delta\hat{V}_{\beta,0}(s)= \frac{L(s)}{2}\left[j\Delta V_1^e(s+j\omega_n)-j\Delta V_1^e(s-j\omega_n)\right. \\ \left.+V_{n,1}\Delta\theta_1^e(s+j\omega_n)+V_{n,1}\Delta\theta_1^e(s-j\omega_n)\right]. \quad (18b)$$

Using (18) and considering the transfer function $L(s)=\frac{k_0}{s+k_0}$, (17) can be rewritten as

$$\begin{bmatrix} U_1(s) \\ U_2(s) \end{bmatrix} = -\frac{1}{2}\begin{bmatrix} L(s-j\omega_n)+L(s+j\omega_n) & \\ \frac{j}{V_{n,1}}\{L(s-j\omega_n)-L(s+j\omega_n)\} & \\ -jV_{n,1}\{L(s-j\omega_n)-L(s+j\omega_n)\} & \\ L(s-j\omega_n)+L(s+j\omega_n) & \end{bmatrix}\begin{bmatrix} \Delta V_1^e(s) \\ \Delta\theta_1^e(s) \end{bmatrix} \\ = \frac{-k_0}{(s+k_0)^2+\omega_n^2}\begin{bmatrix} (s+k_0) & V_{n,1}\omega_n \\ -\omega_n/V_{n,1} & (s+k_0) \end{bmatrix}\begin{bmatrix} \Delta V_1^e(s) \\ \Delta\theta_1^e(s) \end{bmatrix} \quad (19)$$

Based on (19) and the LTP model in Fig. 6, the LTI model of the mROGI-FLL can be obtained as shown in Fig. 10. The LTI model in Fig. 10 is a two-input-two-output (TITO) control system. Therefore, using this model for the analysis and tuning will be more straightforward than the LTP one. This fact is demonstrated in what follows.

Consider a unity-feedback TITO control system as in Fig. 11, where its open-loop transfer matrix is as expressed below:

$$\begin{bmatrix} Y_1(s) \\ Y_2(s) \end{bmatrix} = \underbrace{\begin{bmatrix} p_{11}(s) & p_{12}(s) \\ p_{21}(s) & p_{22}(s) \end{bmatrix}}_{\boldsymbol{P}(s)}\begin{bmatrix} E_1(s) \\ E_2(s) \end{bmatrix}.$$

The characteristic polynomial of the above TITO control system is as (20), where $\det[\boldsymbol{P}(s)]$ and $\mathrm{tr}[\boldsymbol{P}(s)]$ denote the determinant and trace of $\boldsymbol{P}(s)$, respectively [30].

$$1+\overbrace{p_{11}(s)p_{22}(s)-p_{12}(s)p_{21}(s)}^{\det[\boldsymbol{P}(s)]}+\overbrace{p_{11}(s)+p_{22}(s)}^{\mathrm{tr}[\boldsymbol{P}(s)]}=0 \quad (20)$$

The LTI model of the mROGI-FLL, as mentioned before, is also a unity-feedback TITO control system (see Fig. 10). Therefore, its characteristic polynomial can be obtained in a similar manner, as expressed below:

$$s^5+2(k_0+k_1)s^4+(k_0^2+2k_0k_1+k_1^2+\omega_n^2+\lambda)s^3 \\ +(2k_1\omega_n^2+k_0\lambda+k_1\lambda)s^2+(k_1^2+\lambda)\omega_n^2 s+k_1\lambda\omega_n^2=0. \quad (21)$$

Selecting the control parameters and analyzing the stability of the mROGI-FLL are quite straightforward by examining the roots of its characteristic polynomial, which are its closed-loop poles. For instance, to ensure the mROGI-FLL stability, its closed-loop poles should be in the left-half plane, which can be simply determined by examining the roots of (21). The following example better illustrates this fact.

For the sake of study, let us consider a case that the ratios $k_0/k_1=r$ and $\lambda/k_1=\omega_z$ are fixed at $r=1$ and $\omega_z=200$. Fig. 12 shows the location of the roots of (21) in the complex s-plane when k_1 changes in the range of $0<k_1<310$. It is observed that the closed-loop poles of the mROGI-FLL enter the right half-plane and, therefore, make it unstable when $k_1>303.1$. We have studied the same case before in Fig. 8(d) by applying the generalized Nyquist stability criterion to the open-loop HTF of the mROGI-FLL. It is observed that the results of both studies are completely consistent.

D. Model Verification

Here, to evaluate the accuracy of the LTP and LTI models of the mROGI-FLL, some numerical tests are performed. In these tests, as shown in Fig. 13, the α- and β-axis input signals of the mROGI-FLL are generated by considering some small perturbations in the grid voltage parameters. The same perturbations are used as the input signals of the LTP and LTI models of the mROGI-FLL. The results of the mROGI-FLL are then compared with those predicted by its LTP and LTI models.

In this evaluation, the mROGI-FLL and its LTP and LTI models are discretized with a sampling frequency of 10 kHz. The nominal values of the grid voltage parameters are $\omega_n=2\pi 50$ rad/s, $\theta_{n,1}=\int\omega_n dt$, $V_{n,1}=1$ p.u., and $V_{n,0}=0$ p.u. The selected control parameters are $k_0=k_1=100$ and $\lambda=5000$.

Three numerical tests are considered.

- In Test 1, a 10° phase step change happens
- In Test 2, a 0.2 p.u. dc component is suddenly added to the α-axis input.
- In Test 3, a 0.2 p.u. symmetrical voltage sag happens.

Fig. 14 shows the results of these tests. It is observed in these results that the LTP model can accurately predict the transient behavior of the mROGI-FLL in all of its output signals regardless of whether the transient state is caused by a change in the dc component or a parameter of the fundamental component. The LTI model, however, can only predict the transient states in the output phase angle, frequency, and amplitude of the mROGI-FLL if these transients are caused by a change in a parameter of the input fundamental component.

To further investigate, it can be interesting to see how accurate the LTP model is in predicting the stability border of the mROGI-FLL. To this end, the points corresponding to $\omega_z=100$, 200, 300, 400, and 500 on the stability border of the mSOGI-FLL in Fig. 9(b) are considered as the case study (see Table I). These points, which are indicated by k_{1max} in Table I, are the maximum values of k_1 for ensuring the mROGI-FLL stability according to its LTP model. Some digital simulations with different sampling frequencies are conducted to evaluate the accuracy of these theoretical predictions. The obtained results are summarized in Table I. It is observed that there are some small differences between the theoretically predicted and numerically determined k_{1max} when the sampling frequency is 10 kHz. These small differences, however, are considerably

This article has been accepted for publication in a future issue of this journal, but has not been fully edited. Content may change prior to final publication. Citation information: DOI 10.1109/TPEL.2020.3018584, IEEE Transactions on Power Electronics

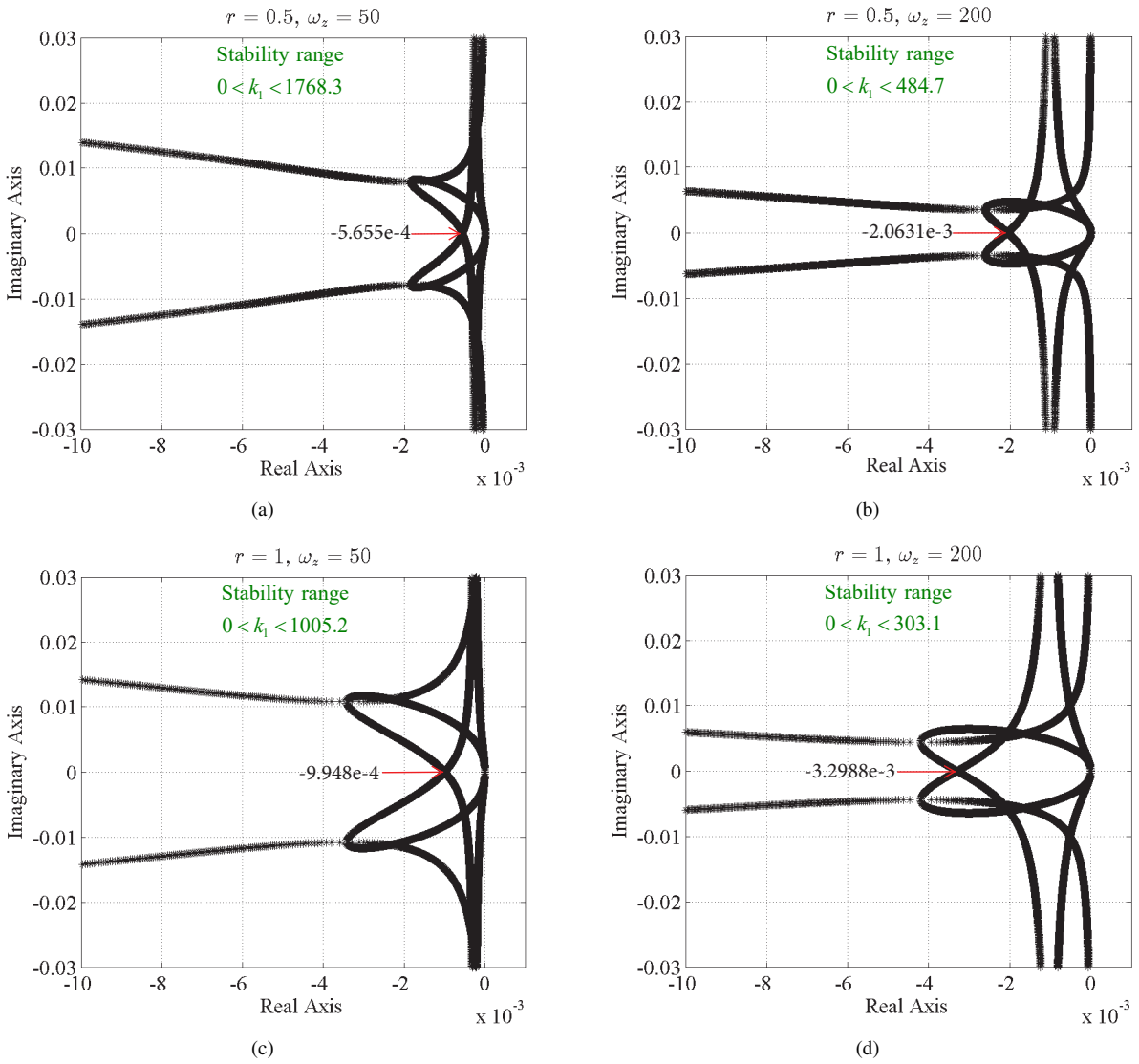

Fig. 8. LTP Nyquist diagrams of the open-loop HTF $G_{\mathcal{HTF}}(s)$ for different sets of control parameters. (a) $r = 0.5$ and $\omega_z = 50$. (b) $r = 0.5$ and $\omega_z = 200$. (c) $r = 1$ and $\omega_z = 50$. (d) $r = 1$ and $\omega_z = 200$.

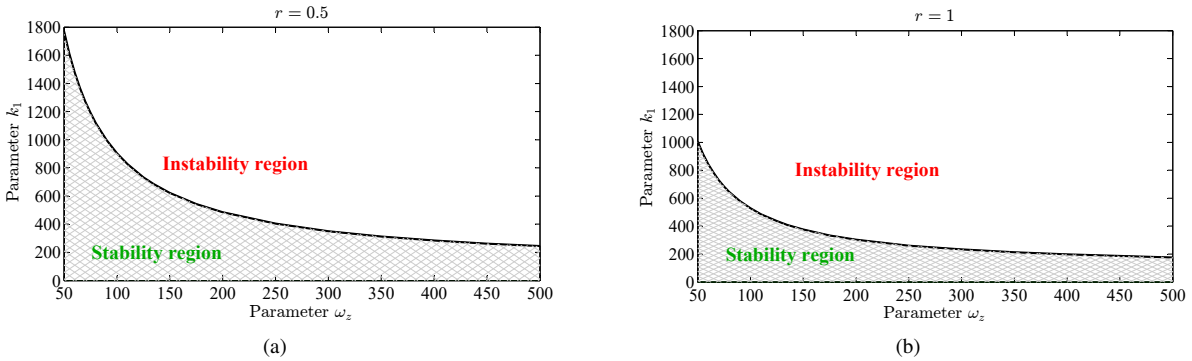

Fig. 9. Stability region of the mROGI-FLL. (a) $r = 0.5$. (b) $r = 1$.

reduced by increasing the sampling frequency. These results were expected as the LTP model and, therefore, its stability-related predictions are based on a continuous-time mROGI-FLL, while the numerical studies and their outcomes are based on a discretized mROGI-FLL. Notice that by increasing the sampling frequency, a discrete system becomes more close to its continuous counterpart.

In addition to the above-mentioned aspects, it should be em-

This article has been accepted for publication in a future issue of this journal, but has not been fully edited. Content may change prior to final publication. Citation information: DOI 10.1109/TPEL.2020.3018584, IEEE Transactions on Power Electronics

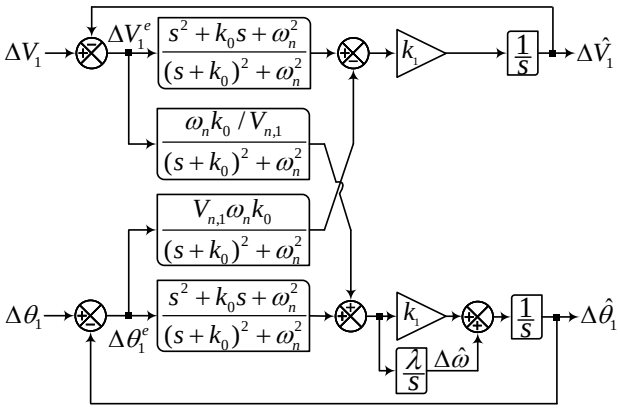

Fig. 10. LTI model of the mROGI-FLL. It will be proved later that this LTI model is also valid for the mSRF-PLL. The only point here is that the control parameters in this model need to be replaced by those of the mSRF-PLL. To be more exact, the control gain k_1 in the upper and lower control loops needs to be replaced by k_v and k_p, respectively, and the control gain λ needs to be replaced by k_i.

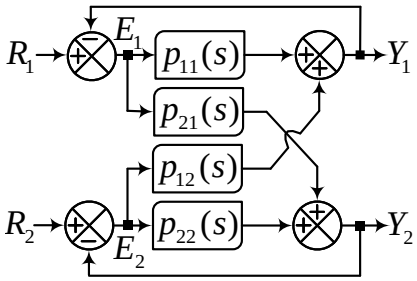

Fig. 11. A unity-feedback TITO control system.

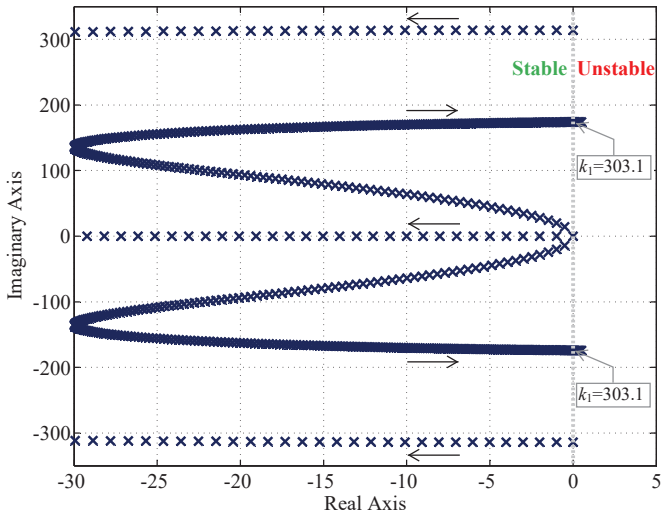

Fig. 12. Changing the location of the closed-loop poles of the mROGI-FLL when k_1 varies in the range of $0 < k_1 < 310$.

phasized here that the LTP and LTI models of the mROGI-FLL are small-signal models at the end of the day. It means that their accuracy tends to decrease by increasing the magnitude of input disturbances. Another important point is that the LTP model only considers the presence of the fundamental and dc components in the input of the mROGI-FLL. It means that this model is not able to predict transient and/or steady-state

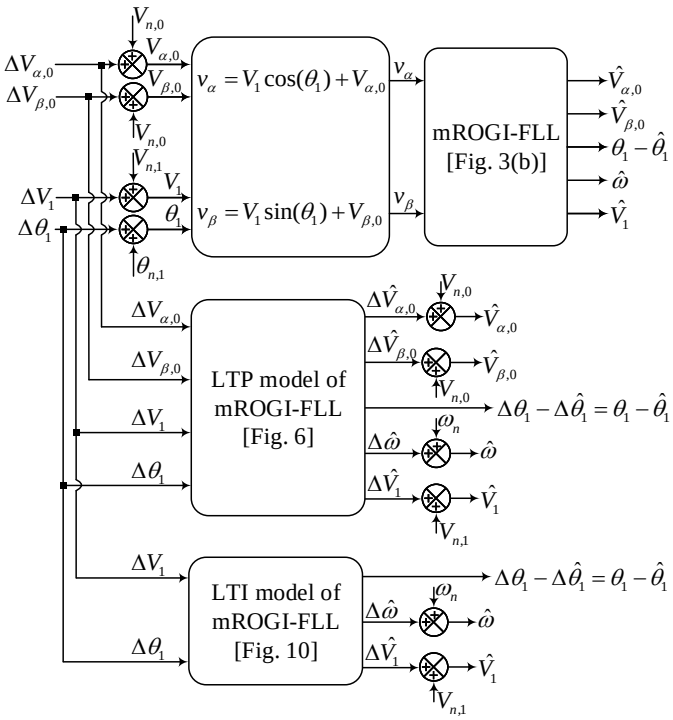

Fig. 13. Schematic diagram of the procedure for the model verification of the mROGI-FLL.

TABLE I
THEORETICALLY PREDICTED AND NUMERICALLY DETERMINED k_{1max} FOR DIFFERENT VALUES OF ω_z

r	ω_z	k_{1max}			
		LTP model	Digital simulation		
			$f_s = 10$ kHz	$f_s = 30$ kHz	$f_s = 50$ kHz
1	100	527.7	555	536	532
1	200	303.1	312	305	304
1	300	232.9	237	234	233
1	400	198	201	199	198
1	500	176.2	179	177	176

effects caused by other frequency components (for example, harmonics, interharmonics, and grid voltage imbalance) in the input of the mROGI-FLL. The LTI model of the mROGI-FLL has also the same limitation.

E. Relationship with mSRF-PLL

The conventional SRF-PLL in Fig. 1(a) has been proven to be mathematically equivalent to the conventional ROGI-FLL in Fig. 3(a) if their control parameters have the following relationship: $k_p = k_v = k_1$ and $k_i = \lambda$ [2]. On the other hand, according to discussions in [31], it is immediate to conclude that the conventional SRF-PLL may also be represented as Fig. 15. Therefore, the conventional ROGI-FLL in Fig. 3(a) is also mathematically equivalent to Fig. 15. Considering this fact, one may conclude that the mSRF-PLL in Fig. 1(b) is mathematically equivalent to the mROGI-FLL in Fig. 3(b) as they are realized by adding the same dc rejection/estimation loops to the basic structures that are mathematically equivalent.

The above conclusion can be verified mathematically by obtaining governing nonlinear differential equations of the

This article has been accepted for publication in a future issue of this journal, but has not been fully edited. Content may change prior to final publication. Citation information: DOI 10.1109/TPEL.2020.3018584, IEEE Transactions on Power Electronics

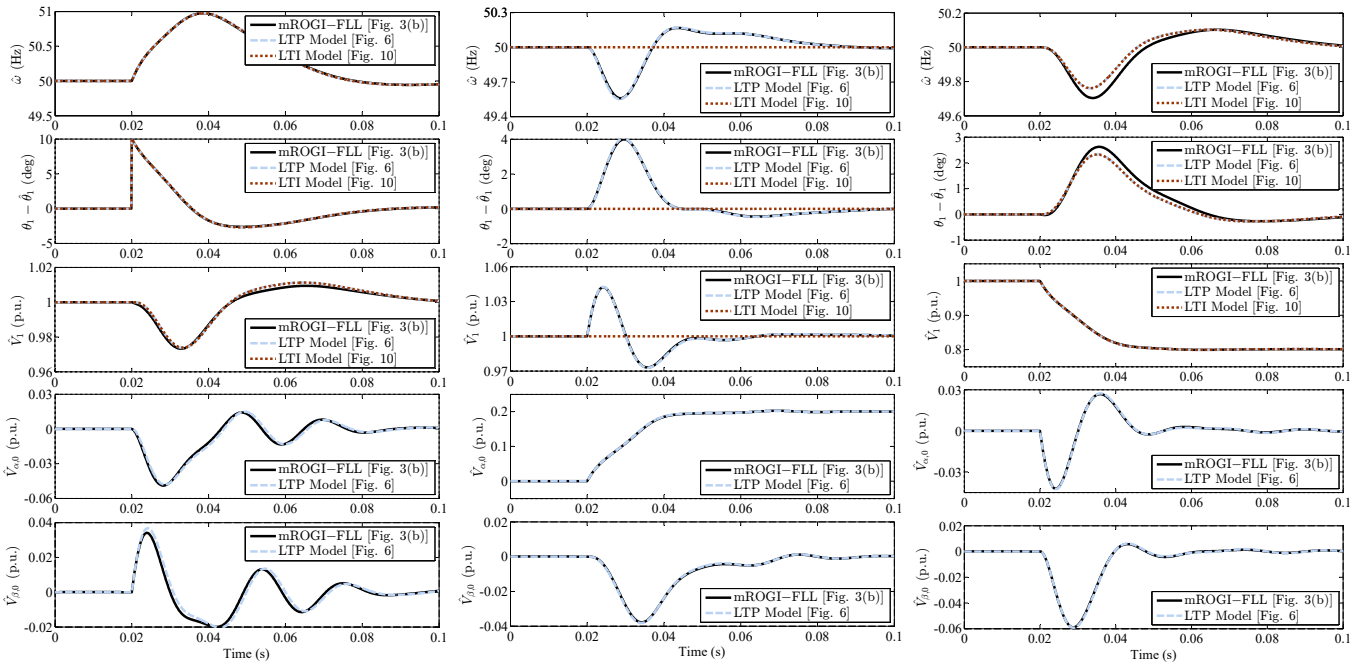

Fig. 14. mROGI-FLL model verification. (a) Test 1: 10° phase angle jump. (b) Test 2: adding 0.2 p.u. dc component to the α-axis input. (c) Test 3: 0.2 p.u. voltage sag.

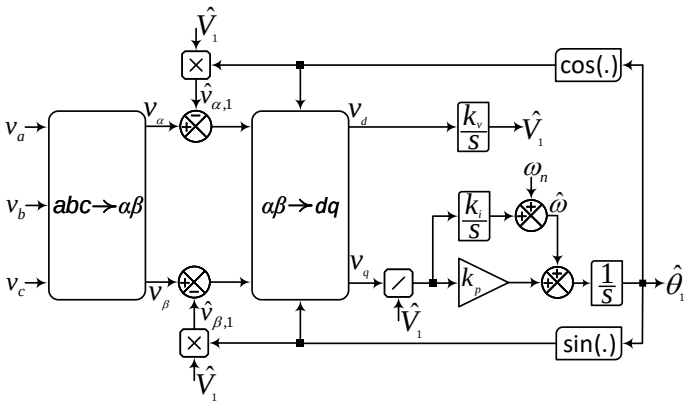

Fig. 15. Alternative representation of the conventional SRF-PLL in Fig. 1(a) [31].

mSRF-PLL and comparing them with those of the mROGI-FLL, which are expressed in (7a)-(7c) and (9), or numerically through some comparative simulation studies. The numerical way is selected here. To this end, some large-signal tests (0.75 p.u. voltage sag and 10 Hz frequency jump tests) are conducted. The results of these tests in Fig. 16 confirm that the mROGI-FLL and mSRF-PLL are mathematically equivalent. Notice that the very small differences between some results are because of discretization errors.

From the equivalence of the mROGI-FLL and mSRF-PLL, it can be concluded that the LTP and LTI models of the mROGI-FLL, which are shown in Fig. 6 and 10, respectively, and all the discussions conducted before based on them are also valid for the mSRF-PLL.

F. Decoupled mROGI-FLL

The LTI model of the mROGI-FLL in Fig. 10 indicates that the amplitude and phase/frequency variables of the mROGI-FLL are dynamically coupled.[3] This fact may also be clearly seen in Fig. 16(a), where a severe voltage sag has caused large spurious transients in the output phase and frequency. The coupling level between the output phase and amplitude of the mROGI-FLL depends on the parameter k_0, which is the control gain of its dc estimation/rejection loop. Reducing the value of k_0 makes the coupling weaker at the cost of slower transient behavior in estimating the dc component. The complete decoupling, from the small-signal point of view, requires $k_0 = 0$, which is not an option here as it corresponds to deactivate the dc offset rejection/estimation loop of the mROGI-FLL. Therefore, an alternative way needs to be found.

Decoupling the amplitude and phase estimation loops of the mROGI-FLL can be carried out in a mathematical or intuitive way. For the sake of brevity, the intuitive way is presented here. A quick look at the solid lines in Fig. 5 shows that the frequency response of the transfer function between the $\alpha\beta$ input signals (v_α and v_β) and the extracted FFPS component (i.e., $\hat{v}_{\alpha,1}$ and $\hat{v}_{\beta,1}$) in the mROGI-FLL is asymmetrical around the fundamental frequency (50 Hz). That is the reason why there is a coupling between the amplitude and phase estimation loops of the mROGI-FLL. In order to decouple these loops, the aforementioned asymmetry in the frequency response needs to be removed. To this end, an additional ROGI centered at

[3]In fact, as the LTP model of the mROGI-FLL in Fig. 6 shows, all parameters (i.e., both the dc and fundamental parameters) in the mROGI-FLL are coupled to each other. However, for the sake of brevity, only the dynamic coupling between the fundamental phase/frequency and amplitude variables is discussed and addressed here.

This article has been accepted for publication in a future issue of this journal, but has not been fully edited. Content may change prior to final publication. Citation information: DOI 10.1109/TPEL.2020.3018584, IEEE Transactions on Power Electronics

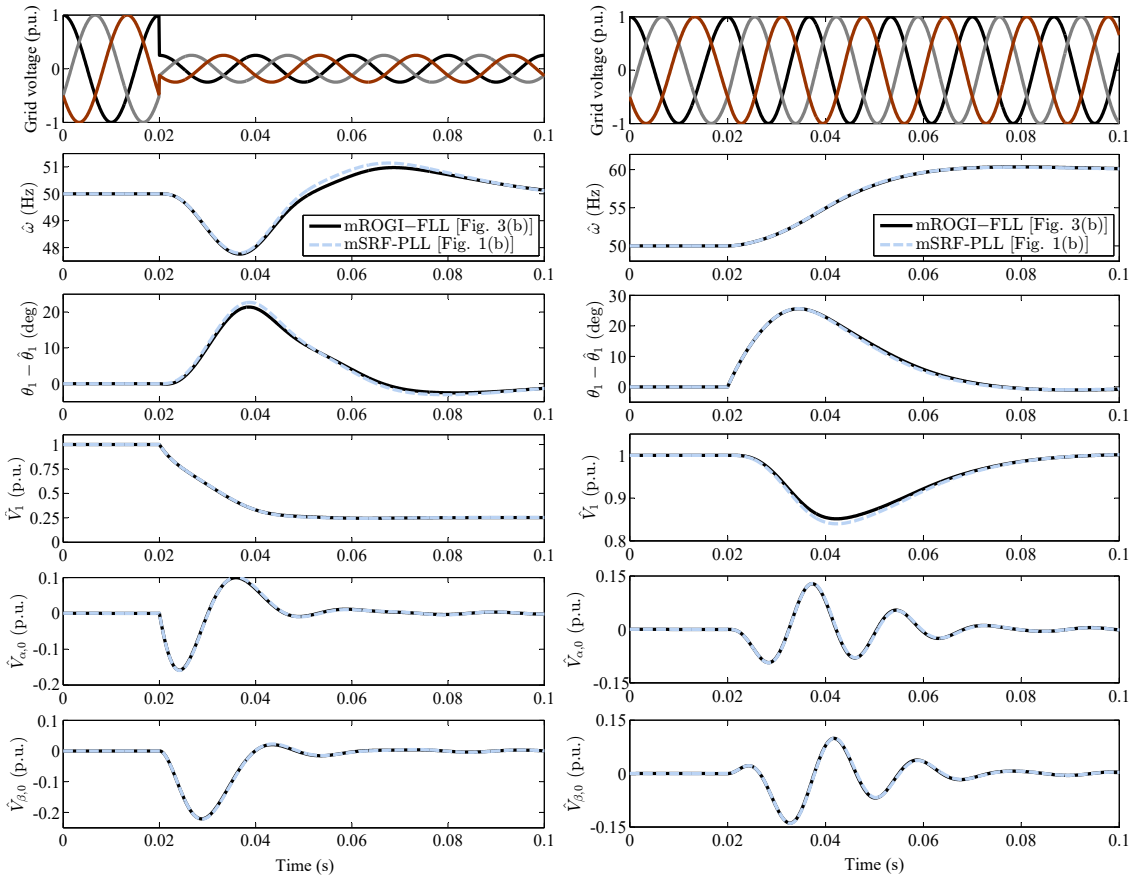

Fig. 16. Performance comparison of the mROGI-FLL and mSRF-PLL. (a) 0.75 p.u. voltage sag. (b) 10 Hz frequency jump. The disturbances, especially the frequency jump, are exaggeratedly large to prove that the mROGI-FLL and mSRF-PLL, not only from the small-signal point of view, but also from the large-signal point of view are mathematically equivalent. The control parameters are: $k_1 = k_0 = k_v = k_p = 100$ and $\lambda = k_i = 5000$.

twice the fundamental grid frequency can be added to the mROGI-FLL, as shown in Fig. 17. The resulting structure is called the decoupled mROGI-FLL because, as dashed lines in Fig. 5 shows, it has a symmetrical frequency response around the fundamental grid frequency and, consequently, a highly decoupled phase/amplitude estimation dynamics. To support this fact, a comparison between the mROGI-FLL and the decoupled mROGI-FLL under the same voltage sag test as in Fig. 16(a) is carried out. The results of this test in Fig. 18 show that the spurious transients in the output phase and frequency of the decoupled mROGI-FLL are negligible compared to those in the mROGI-FLL. It confirms that the amplitude and phase/frequency estimation dynamics of the decoupled mROGI-FLL are highly decoupled. It is worth mentioning here that decoupling the phase/frequency and amplitude estimation loops of the mSRF-PLL may also be carried out in a similar manner.

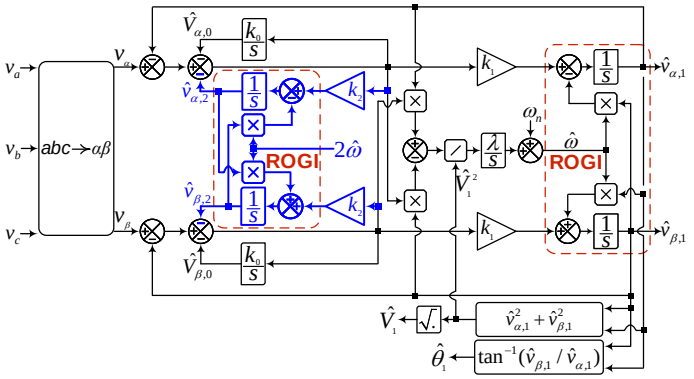

Fig. 17. Decoupled mROGI-FLL. The control parameter k_2 should be selected equal to k_0.

III. Modified SOGI-FLL (mSOGI-FLL)

A. LTP Modeling

1) Assumptions: For the LTP modeling of the mSOGI-FLL in Fig. 4(b), it is assumed that its single-phase input contains a fundamental component and a dc component, as expressed in (22), in which V_1 and θ_1 are the amplitude and phase angle of the fundamental component, respectively, and V_0 denotes the dc component.

$$v(t) = V_1 \cos(\theta_1) + V_0 \tag{22}$$

If we assume that the estimated frequency $\hat{\omega}$ in Fig. 4(b) is a constant, the characteristic transfer functions between the output signals $\hat{v}_1$ and $\hat{v}_1'$ and the input signal v can be obtained

This article has been accepted for publication in a future issue of this journal, but has not been fully edited. Content may change prior to final publication. Citation information: DOI 10.1109/TPEL.2020.3018584, IEEE Transactions on Power Electronics

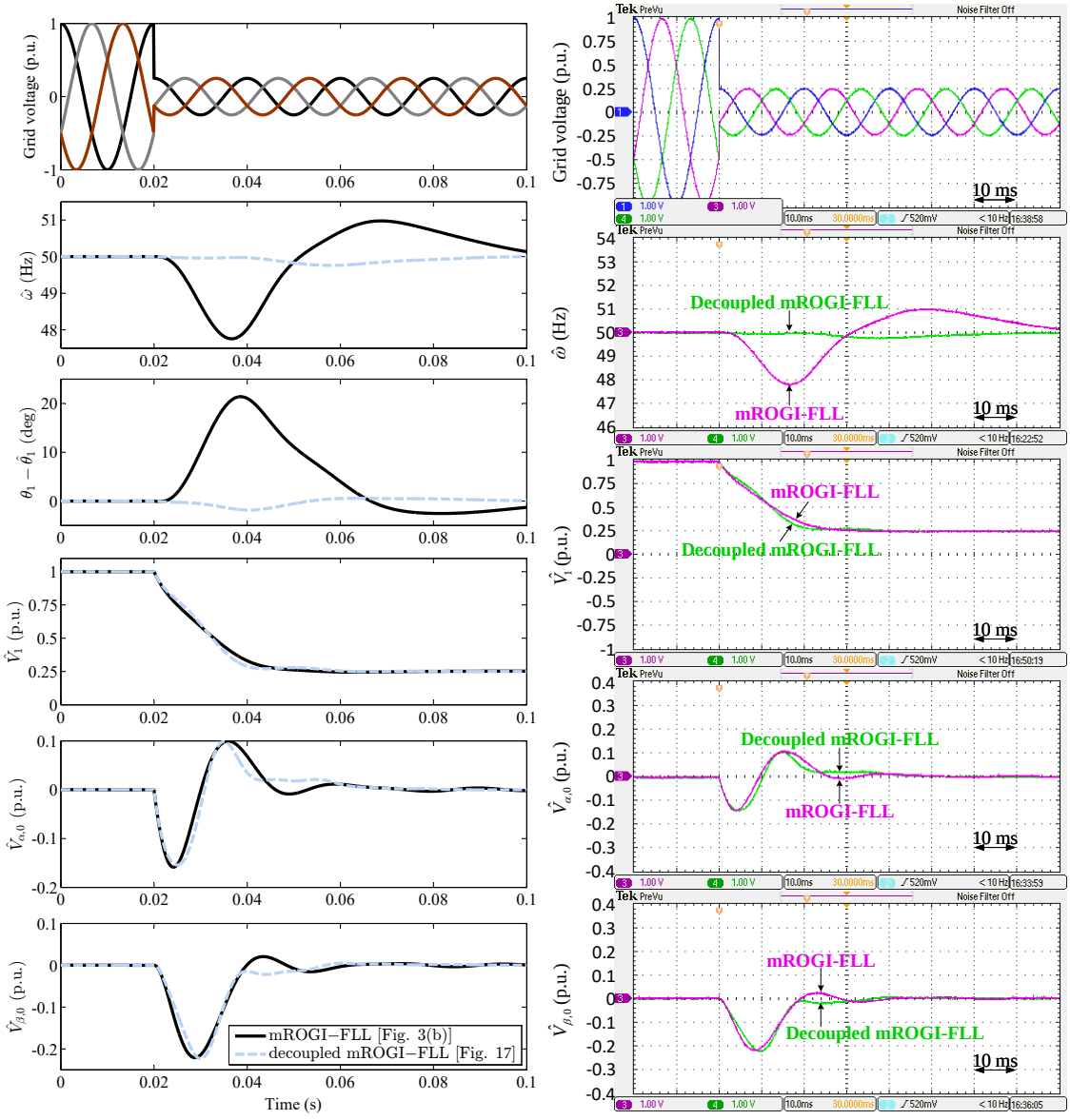

(a) (b)

Fig. 18. A comparison between the mROGI-FLL and decoupled mROGI-FLL under 0.75 p.u. voltage sag. (a) Simulation results. (b) Experimental results. Control parameters: $k_0 = k_1 = k_2 = 100$ and $\lambda = 5000$. In the experimental result, which are obtained using the Chroma grid simulator 61845, dSPACE 1006 platform, and Tektronix digital oscilloscope DPO 2014B, the phase error signal cannot be shown as the actual phase angle is unknown.

as

$$\hat{v}_1(s) = \overbrace{\frac{k_1\hat{\omega}s^2}{s^3 + (k_0 + k_1\hat{\omega})s^2 + \hat{\omega}^2 s + k_0\hat{\omega}^2}}^{G_1(s)} v(s) \quad (23a)$$

$$\hat{v}'_1(s) = \underbrace{\frac{k_1\hat{\omega}^2 s}{s^3 + (k_0 + k_1\hat{\omega})s^2 + \hat{\omega}^2 s + k_0\hat{\omega}^2}}_{G'_1(s)} v(s). \quad (23b)$$

Both these transfer functions have a zero at the origin. It means that the output signals $\hat{v}_1$ and $\hat{v}'_1$ in the mSOGI-FLL are free from any dc component in the steady state. Besides, it can be shown that $|G_1(j\hat{\omega})|\angle G_1(j\hat{\omega}) = 1\angle 0°$ and $|G'_1(j\hat{\omega})|\angle G'_1(j\hat{\omega}) = 1\angle -90°$. Considering these facts, the output signals $\hat{v}_1$ and $\hat{v}'_1$ in the mSOGI-FLL structure can be considered as an estimation of the fundamental component of the input signal v and its 90° phase shifted version, as expressed below:

$$\hat{v}_1(t) = \hat{V}_1 \cos(\hat{\theta}_1) \quad (24a)$$

$$\hat{v}'_1(t) = \hat{V}_1 \sin(\hat{\theta}_1). \quad (24b)$$

Notice that $\hat{V}_1$ and $\hat{\theta}_1$ in (24) are the estimations of V_1 and θ_1 in (22), respectively.

It is also assumed that the mSOGI-FLL operates in a quasi-locked state, which is corresponding to $\hat{V}_1 \approx V_1$, $\hat{\theta}_1 \approx \theta_1$, $\hat{\omega} \approx \omega$, and $\hat{V}_0 \approx V_0$. All these parameters are also defined as (25), where Δ and the subscript n denote a small perturbation

This article has been accepted for publication in a future issue of this journal, but has not been fully edited. Content may change prior to final publication. Citation information: DOI 10.1109/TPEL.2020.3018584, IEEE Transactions on Power Electronics

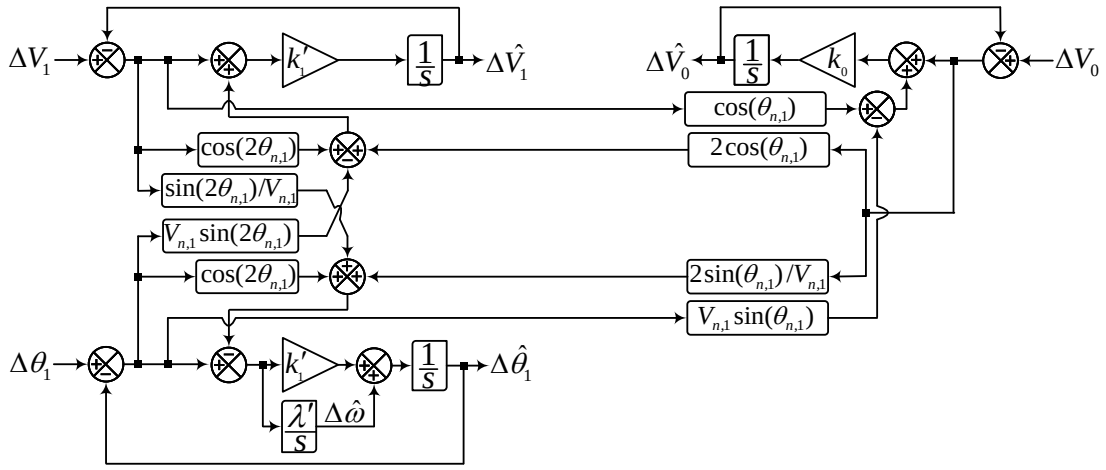

Fig. 19. LTP model of the mSOGI-FLL. $k_1' = k_1\omega_n/2$ and $\lambda' = \lambda/2$. It will be proved later that this LTP model is valid for the mEPLL too. The only point here is that the gain $k_1' = k_1\omega_n/2$ in the upper and lower control loops needs to be replaced by $k_v/2$ and $k_p/2$, respectively, and gain $\lambda' = \lambda/2$ needs to be replaced by $k_i/2$.

and a nominal value, respectively.

$$\begin{aligned} \hat{V}_0 &= V_{n,0} + \Delta\hat{V}_0, \quad & V_0 &= V_{n,0} + \Delta V_0 \\ \hat{V}_1 &= V_{n,1} + \Delta\hat{V}_1, \quad & V_1 &= V_{n,1} + \Delta V_1 \\ \hat{\theta}_1 &= \theta_{n,1} + \Delta\hat{\theta}_1, \quad & \theta_1 &= \theta_{n,1} + \Delta\theta_1 \\ \hat{\omega} &= \omega_n + \Delta\hat{\omega}, \quad & \omega &= \omega_n + \Delta\omega. \end{aligned} \tag{25}$$

2) Governing Nonlinear Differential Equations: From Fig. 4(b), the estimated parameters by the mSOGI-FLL can be expressed as

$$\hat{V}_0 = k_0 \int (v - \hat{v}_1 - \hat{V}_0)dt \tag{26a}$$

$$\hat{\omega} = \omega_n - \lambda \int \frac{(v - \hat{v}_1 - \hat{V}_0)\hat{v}_1'}{\hat{V}_1^2}dt \tag{26b}$$

$$\hat{\theta}_1 = \tan^{-1}\left(\frac{\hat{v}_1'}{\hat{v}_1}\right) \tag{26c}$$

$$\hat{V}_1 = \sqrt{\hat{v}_1^2 + \hat{v}_1'^2}. \tag{26d}$$

Differentiating from (26) with respect to time results in

$$\frac{d\hat{V}_0}{dt} = k_0(v - \hat{v}_1 - \hat{V}_0) \tag{27a}$$

$$\frac{d\hat{\omega}}{dt} = -\frac{\lambda}{\hat{V}_1^2}(v - \hat{v}_1 - \hat{V}_0)\hat{v}_1' \tag{27b}$$

$$\frac{d\hat{\theta}_1}{dt} = \frac{\hat{v}_1\frac{d\hat{v}_1'}{dt} - \hat{v}_1'\frac{d\hat{v}_1}{dt}}{\hat{V}_1^2} \tag{27c}$$

$$\frac{d\hat{V}_1}{dt} = \frac{\hat{v}_1\frac{d\hat{v}_1}{dt} + \hat{v}_1'\frac{d\hat{v}_1'}{dt}}{\hat{V}_1} \tag{27d}$$

in which the time derivatives $\frac{d\hat{v}_1}{dt}$ and $\frac{d\hat{v}_1'}{dt}$, according to Fig. 4(b), are equal to

$$\frac{d\hat{v}_1}{dt} = -\hat{\omega}\hat{v}_1' + k_1\hat{\omega}(v - \hat{v}_1 - \hat{V}_0) \tag{28a}$$

$$\frac{d\hat{v}_1'}{dt} = \hat{\omega}\hat{v}_1. \tag{28b}$$

Considering (28), the equations (27c) and (27d) can be rewritten as

$$\frac{d\hat{\theta}_1}{dt} = \frac{\hat{\omega}(\hat{v}_1^2 + \hat{v}_1'^2) - k_1\hat{\omega}\overbrace{(v - \hat{v}_1 - \hat{V}_0)\hat{v}_1'}^{-\frac{\hat{V}_1^2}{\lambda}\frac{d\hat{\omega}}{dt}}}{\hat{V}_1^2} \tag{29a}$$

$$\frac{d\hat{V}_1}{dt} = k_1\hat{\omega}\frac{(v - \hat{v}_1 - \hat{V}_0)\hat{v}_1}{\hat{V}_1}. \tag{29b}$$

Replacing the signals v, $\hat{v}_1$ and $\hat{v}_1'$ in (27a), (27b), and (29) with (22), (24a), and (24b) yields the governing nonlinear differential equations of the mSOGI-FLL as follows:

$$\frac{d\hat{V}_0}{dt} = k_0\left[V_1\cos(\theta_1) + V_0 - \hat{V}_1\cos(\hat{\theta}_1) - \hat{V}_0\right] \tag{30a}$$

$$\begin{aligned} \frac{d\hat{\omega}}{dt} &= -\frac{\lambda}{\hat{V}_1}\left[V_1\cos(\theta_1) + V_0 - \hat{V}_1\cos(\hat{\theta}_1) - \hat{V}_0\right]\sin(\hat{\theta}_1) \\ &= \frac{\lambda}{2\hat{V}_1}\Big[V_1\sin(\theta_1 - \hat{\theta}_1) - V_1\sin(\theta_1 + \hat{\theta}_1) \\ &\qquad + \hat{V}_1\sin(2\hat{\theta}_1) - 2(V_0 - \hat{V}_0)\sin(\hat{\theta}_1)\Big] \end{aligned} \tag{30b}$$

$$\frac{d\hat{\theta}_1}{dt} = \hat{\omega} + \frac{k_1\hat{\omega}}{\lambda}\frac{d\hat{\omega}}{dt} \tag{30c}$$

$$\begin{aligned} \frac{d\hat{V}_1}{dt} &= k_1\hat{\omega}\left[V_1\cos(\theta_1) + V_0 - \hat{V}_1\cos(\hat{\theta}_1) - \hat{V}_0\right]\cos(\hat{\theta}_1) \\ &= \frac{k_1\hat{\omega}}{2}\Big[V_1\cos(\theta_1 - \hat{\theta}_1) + V_1\cos(\theta_1 + \hat{\theta}_1) - \hat{V}_1 \\ &\qquad - \hat{V}_1\cos(2\hat{\theta}_1) + 2(V_0 - \hat{V}_0)\cos(\hat{\theta}_1)\Big]. \end{aligned} \tag{30d}$$

3) Linearization: By replacing the actual and estimated parameters in (30) by their nominal values plus a small perturbation, as defined in (25), and linearizing the resulting equations in a similar manner as done before in Section II-A3 [see (11)], we can obtain (31) at the top of the next page. These equations are a set of LTP differential equations, which describe the mSOGI-FLL dynamics. Using these equations, the LTP model of the mSOGI-FLL can be obtained, as shown in Fig. 19. Using this LTP model and by following

This article has been accepted for publication in a future issue of this journal, but has not been fully edited. Content may change prior to final publication. Citation information: DOI 10.1109/TPEL.2020.3018584, IEEE Transactions on Power Electronics

$$\frac{d\Delta\hat{V}_0}{dt} \approx k_0 \left[(\Delta V_1 - \Delta\hat{V}_1)\cos(\theta_{n,1}) - V_{n,1}(\Delta\theta_1 - \Delta\hat{\theta}_1)\sin(\theta_{n,1}) + \Delta V_0 - \Delta\hat{V}_0 \right] \tag{31a}$$

$$\frac{d\Delta\hat{\omega}}{dt} \approx \frac{\lambda}{2V_{n,1}} \left[V_{n,1}\left\{1 - \cos(2\theta_{n,1})\right\}(\Delta\theta_1 - \Delta\hat{\theta}_1) - (\Delta V_1 - \Delta\hat{V}_1)\sin(2\theta_{n,1}) - 2(\Delta V_0 - \Delta\hat{V}_0)\sin(\theta_{n,1}) \right] \tag{31b}$$

$$\frac{d\Delta\hat{\theta}_1}{dt} \approx \Delta\hat{\omega} + \frac{k_1\omega_n}{\lambda}\frac{d\Delta\hat{\omega}}{dt} \tag{31c}$$

$$\frac{d\Delta V_1}{dt} \approx \frac{k_1\omega_n}{2} \left[\left\{1 + \cos(2\theta_{n,1})\right\}(\Delta V_1 - \Delta\hat{V}_1) - V_{n,1}\sin(2\theta_{n,1})(\Delta\theta_1 - \Delta\hat{\theta}_1) + 2(\Delta V_0 - \Delta\hat{V}_0)\cos(\theta_{n,1}) \right] \tag{31d}$$

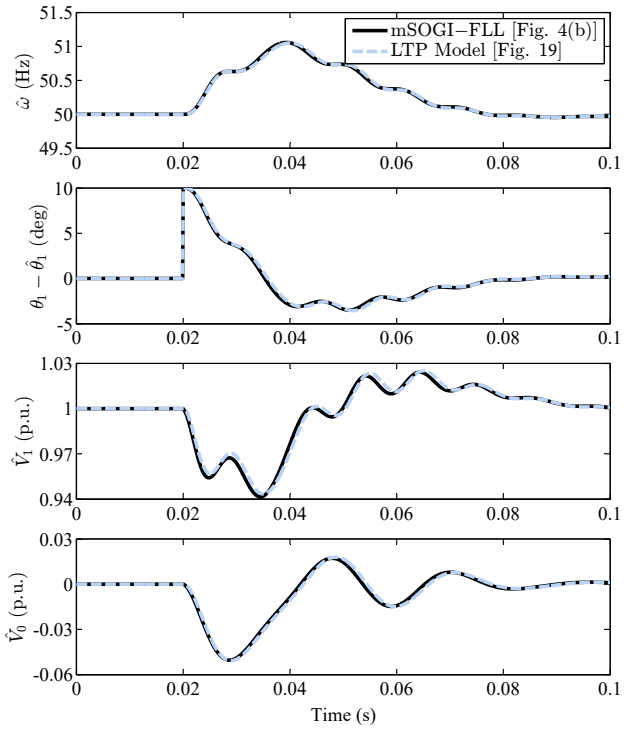

Fig. 20. mSOGI-FLL model verification in response to a 10° phase angle jump.

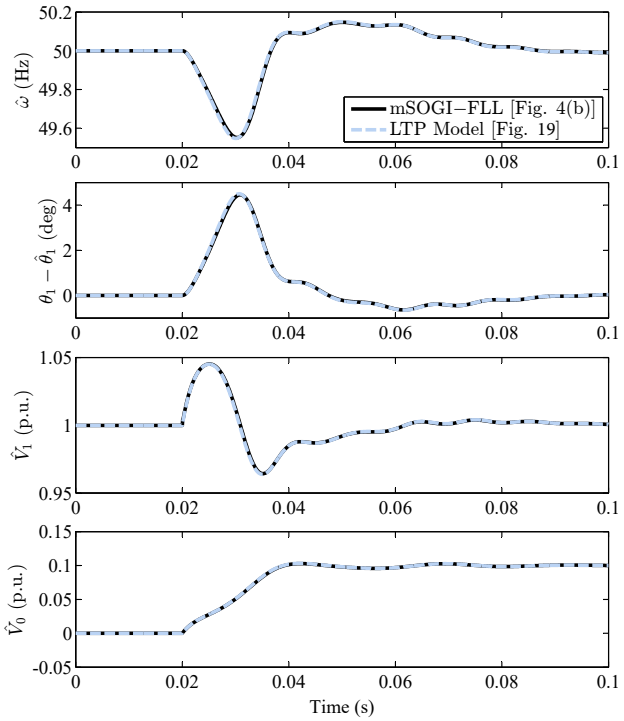

Fig. 21. mSOGI-FLL model verification in response to adding 0.1 p.u. dc component to the grid voltage.

a more or less similar manner as that explained before for the mROGI-FLL, the mSOGI-FLL stability and dynamics can be investigated.

B. Model Verification

By following a similar procedure as that described in Section II-D, the accuracy of the LTP model of the mSOGI-FLL is investigated. Here, two tests are considered. The first one is a 10° phase jump test, and the second one is a step change in the input dc component from zero to 0.1 p.u. Figs. 20 and 21, which are the results of these tests, confirm the high accuracy of the derived LTP model.

C. Relationship with mEPLL

It has been discussed and proven in the literature [1], [18], [32] that the EPLL and SOGI-FLL are mathematically equivalent systems if the following relationship between their control parameters is hold: $k_v = k_p = k_1\omega_n$ and $k_i = \lambda$. It means that the mEPLL and mSOGI-FLL, which are realized by adding a simple integrator to the EPLL and SOGI-FLL, respectively, are also mathematically equivalent. Therefore, it can be concluded that the mSOGI-FLL LTP model in Fig. 19 is also valid for the mEPLL. These facts can be verified using numerical tests. To save space, the numerical results are not shown here.

IV. Conclusions

Modeling and analysis of three-phase and single-phase grid synchronization systems with the dc component rejection/estimation capability was the main objective of this paper. The mROGI-FLL, mSRF-PLL, mSOGI-FLL, and mEPLL were considered as case studies. The focus of the study was first on the mROGI-FLL. Through a step-by-step mathematical procedure, an LTP model for the mROGI-FLL was derived. It was then shown how the open-loop HTF of the mROGI-FLL can be obtained using its LTP model, and how by applying the generalized Nyquist criterion, its stability can be analyzed.

An LTI model, which is a special case of its LTP model, was also presented for the mROGI-FLL. It was discussed that this LTI model may facilitate the mROGI-FLL analysis at the cost of the inability in predicting some dynamics of the mROGI-FLL. It was also demonstrated that the mSRF-PLL is mathematically equivalent to the mROGI-FLL. Based on this equivalence, it was concluded that the LTP and LTI models of the mROGI-FLL are valid for the mSRF-PLL. In addition, the dynamic coupling between the phase/frequency and amplitude estimation loops of the mROGI-FLL was discussed, and a simple yet efficient approach to decouple these loops was proposed.

For the case of the mSOGI-FLL, by following a similar procedure as the case of mROGI-FLL, an LTP model was derived, and its accuracy was confirmed using numerical tests. It was also discussed that this model is valid for the mEPLL as this PLL is mathematically equivalent to the mSOGI-FLL.

This paper makes a valuable contribution to the field of grid synchronization and paves the way towards the LTP modeling and analysis of more sophisticated synchronization systems as the available works in this area are limited.

ACKNOWLEDGMENT

The authors acknowledge with thanks technical and financial supports of The DSR and The Villum Foundation.

REFERENCES

[1] S. Golestan, J. M. Guerrero, F. Musavi, and J. C. Vasquez, "Single-phase frequency-locked loops: A comprehensive review," *IEEE Trans. Power Electron.*, vol. 34, no. 12, pp. 11 791–11 812, Dec. 2019.

[2] S. Golestan, J. M. Guerrero, J. C. Vasquez, A. M. Abusorrah, and Y. Al-Turki, "A study on three-phase FLLs," *IEEE Trans. Power Electron.*, vol. 34, no. 1, pp. 213–224, Jan. 2019.

[3] S. Golestan, J. M. Guerrero, and J. C. Vasquez, "Three-phase PLLs: A review of recent advances," *IEEE Trans. Power Electron.*, vol. 32, no. 3, pp. 1894–1907, Mar. 2017.

[4] S. Golestan, J. M. Guerrero, and J. C. Vasquez, "Single-phase PLLs: A review of recent advances," *IEEE Trans. Power Electron.*, vol. 32, no. 12, pp. 9013–9030, Dec. 2017.

[5] V. Kaura and V. Blasko, "Operation of a phase locked loop system under distorted utility conditions," *IEEE Trans. Ind. Appl.*, vol. 33, no. 1, pp. 58–63, Jan. 1997.

[6] S.-K. Chung, "A phase tracking system for three phase utility interface inverters," *IEEE Trans. Power Electron.*, vol. 15, no. 3, pp. 431–438, May. 2000.

[7] T. Thacker, D. Boroyevich, R. Burgos, and F. Wang, "Phase-locked loop noise reduction via phase detector implementation for single-phase systems," *IEEE Trans. Ind. Electron.*, vol. 58, no. 6, pp. 2482–2490, Jun. 2011.

[8] F. Xiao, L. Dong, L. Li, and X. Liao, "A frequency-fixed SOGI-based PLL for single-phase grid-connected converters," *IEEE Trans. Power Electron.*, vol. 32, no. 3, pp. 1713–1719, Mar. 2017.

[9] P. Lamo, F. Lopez, A. Pigazo, and F. J. Azcondo, "An efficient FPGA implementation of a quadrature signal-generation subsystem in SRF PLLs in single-phase PFCs," *IEEE Trans. Power Electron.*, vol. 32, no. 5, pp. 3959–3969, May. 2017.

[10] X. Fang, Y. Wang, M. Li, and J. Liu, "A novel frequency-adaptive PLL for single-phase grid-connected converters," in *2010 IEEE Energy Convers. Congr. Expo.*, Sep. 2010, pp. 414–419.

[11] M. Karimi-Ghartemani, "A unifying approach to single-phase synchronous reference frame PLLs," *IEEE Trans. Power Electron.*, vol. 28, no. 10, pp. 4550–4556, Oct. 2013.

[12] Z. Xin, R. Zhao, P. Mattavelli, P. C. Loh, and F. Blaabjerg, "Re-investigation of generalized integrator based filters from a first-order-system perspective," *IEEE Access*, vol. 4, pp. 7131–7144, 2016.

[13] S. G. Jorge, C. A. Busada, and J. A. Solsona, "Frequency adaptive discrete filter for grid synchronization under distorted voltages," *IEEE Trans. Power Electron.*, vol. 27, no. 8, pp. 3584–3594, Aug. 2012.

[14] X. Q. Guo, "Frequency-adaptive voltage sequence estimation for grid synchronisation," *Electronics Letters*, vol. 46, no. 14, pp. 980–982, Jul. 2010.

[15] X. Q. Guo and W. Y. Wu, "Simple synchronisation technique for three-phase grid-connected distributed generation systems," *IET Renew. Power Gen.*, vol. 7, no. 1, pp. 55–62, Feb. 2013.

[16] W. Li, X. Ruan, C. Bao, D. Pan, and X. Wang, "Grid synchronization systems of three-phase grid-connected power converters: A complex-vector-filter perspective," *IEEE Trans. Ind. Electron.*, vol. 61, no. 4, pp. 1855–1870, Apr. 2014.

[17] P. Rodriguez, A. Luna, I. Candela, R. Mujal, R. Teodorescu, and F. Blaabjerg, "Multiresonant frequency-locked loop for grid synchronization of power converters under distorted grid conditions," *IEEE Trans. Ind. Electron.*, vol. 58, no. 1, pp. 127–138, Jan. 2011.

[18] M. Karimi-Ghartemani, S. A. Khajehoddin, P. K. Jain, A. Bakhshai, and M. Mojiri, "Addressing DC component in PLL and notch filter algorithms," *IEEE Trans. Power Electron.*, vol. 27, no. 1, pp. 78–86, Jan. 2012.

[19] S. Golestan, J. M. Guerrero, and G. B. Gharehpetian, "Five approaches to deal with problem of DC offset in phase-locked loop algorithms: Design considerations and performance evaluations," *IEEE Trans. Power Electron.*, vol. 31, no. 1, pp. 648–661, Jan. 2016.

[20] S. Golestan, J. M. Guerrero, and J. C. Vasquez, "DC-offset rejection in phase-locked loops: A novel approach," *IEEE Trans. Ind. Electron.*, vol. 63, no. 8, pp. 4942–4946, 2016.

[21] F. Wu, D. Sun, L. Zhang, and J. Duan, "Influence of plugging DC offset estimation integrator in single-phase EPLL and alternative scheme to eliminate effect of input DC offset and harmonics," *IEEE Trans. Ind. Electron.*, vol. 62, no. 8, pp. 4823–4831, Aug. 2015.

[22] J. Matas, M. Castilla, J. Miret, L. G. de Vicuña, and R. Guzman, "An adaptive prefiltering method to improve the speed/accuracy tradeoff of voltage sequence detection methods under adverse grid conditions," *IEEE Trans. Ind. Electron.*, vol. 61, no. 5, pp. 2139–2151, May. 2014.

[23] Z. Xin, X. Wang, Z. Qin, M. Lu, P. C. Loh, and F. Blaabjerg, "An improved second-order generalized integrator based quadrature signal generator," *IEEE Trans. Power Electron.*, vol. 31, no. 12, pp. 8068–8073, 2016.

[24] M. Karimi-Ghartemani, S. A. Khajehoddin, P. Jain, and A. Bakhshai, "Comparison of two methods for addressing DC component in phase-locked loop (PLL) systems," in *2011 IEEE Energy Conversion Congress and Exposition*, 2011, pp. 3053–3058.

[25] G. Buticchi and E. Lorenzani, "Detection method of the DC bias in distribution power transformers," *IEEE Trans. Ind. Electron.*, vol. 60, no. 8, pp. 3539–3549, 2013.

[26] G. Buticchi, E. Lorenzani, and G. Franceschini, "A DC offset current compensation strategy in transformerless grid-connected power converters," *IEEE Trans. Power Del.*, vol. 26, no. 4, pp. 2743–2751, 2011.

[27] S. R. Hall and N. M. Wereley, "Generalized Nyquist stability criterion for linear time periodic systems," in *1990 American Control Conference*, May. 1990, pp. 1518–1525.

[28] E. Mollerstedt and B. Bernhardsson, "Out of control because of harmonics-An analysis of the harmonic response of an inverter locomotive," *IEEE Contr. Syst. Mag.*, vol. 20, no. 4, pp. 70–81, Aug. 2000.

[29] S. Golestan, J. M. Guerrero, J. C. Vasquez, A. M. Abusorrah, and Y. A. Al-Turki, "Standard SOGI-FLL and its close variants: Precise modeling in LTP framework and determining stability region/robustness metrics," *IEEE Trans. Power Electron.*, vol. PP, no. 99, pp. 1–12, 2020.

[30] M. Pachter, T. Kobylarz, and C. Houpis, "Literal Nyquist stability criterion for MIMO control systems," *Int. J. Control*, vol. 63, no. 1, pp. 55–65, 1996.

[31] M. Karimi-Ghartemani, "A novel three-phase magnitude-phase-locked loop system," *IEEE Trans. Circuits Syst. I, Reg. Papers*, vol. 53, no. 8, pp. 1792–1802, Aug. 2006.

[32] M. Karimi-Ghartemani, "Linear and pseudolinear enhanced phased-locked loop (EPLL) structures," *IEEE Trans. Ind. Electron.*, vol. 61, no. 3, pp. 1464–1474, Mar. 2014.